International Journal of Plasticity 172 (2024) 103854

Contents lists available at ScienceDirect

International Journal of Plasticity

journal homepage: www.elsevier.com/locate/ijplas

Effect of grain boundary misorientation and carbide precipitation on damage initiation: A coupled crystal plasticity and phase field *damage* study

Michael Salvini [a,*,1], Nicolò Grilli [a,1], Eralp Demir [c], Siqi He [b,e], Tomas Martin [b], Peter Flewitt [b], Mahmoud Mostafavi [a], Christopher Truman [a], David Knowles [a,d]

[a] *Department of Electrical, Electronics and Mechanical Engineering, University of Bristol, BS8 1TR, UK*
[b] *Department of Physics, University of Bristol, BS8 1TL, UK*
[c] *Department of Engineering Science, University of Oxford, OX1 3PJ, UK*
[d] *Henry Royce Institute, Manchester, M13 9PL, UK*
[e] *Atkins, Bristol, BS32 4RZ, UK*

ARTICLE INFO

Keywords:
Crystal plasticity
Phase-field damage
Plasticity
316H austenitic stainless steel
Damage
Electron backscatter diffraction
Electron microscopy
Cavity nucleation
Damage initiation
Grain boundary misorientation

ABSTRACT

A coupled crystal plasticity phase field damage framework has been developed and applied to modelling damage initiation. A novel implementation of a grain misorientation angle dependent critical energy release rate has been used to determine a reduction in the local critical energy release rate resulting from the effects of intergranular carbide precipitates and grain boundary misorientation. When applied to a notched high temperature 316H austenitic stainless steel specimen, a good correlation between experimental results and void nucleation statistics for a misorientation dependent critical energy release rate was obtained. This has been evaluated through comparison with correlative electron microscopy experimental results, showing the potential of phase field models in the area of early damage formation. Additions to include plastic strain and creep deformation effects were made, and comparisons were drawn with experimental data to investigate the contributions of microstructural geometry properties such as the difference in and average values of Schmid factors across grain boundaries, as well as the loading direction stress and dislocation densities. The limitations to this approach and opportunities for further work in this area are discussed, with specific interest in the need for additional literature data characterising grain boundary carbide precipitation and cavity nucleation analysis.

1. Introduction

A key target for improving the economics of existing nuclear fission reactor power station projects is extending their operational lifetime. The 60-year design of the next generation of electrical power generation nuclear power plants will integrate predictive modelling techniques combined with targeted in-service testing, monitoring, and maintenance to reduce operational outages (Xiao et al., 2022; Gupta and Bronkhorst, 2021; Zinkle and Was, 2013). Headers, boiler tubes, welded joints, and other structural components in the primary and secondary circuits are made of stainless steel and are subjected to high temperatures and pressures

---

[*] Corresponding author.
E-mail address: michael.salvini.2016@bristol.ac.uk (M. Salvini).
[1] Authors contributed equally.

https://doi.org/10.1016/j.ijplas.2023.103854
Received 20 July 2023; Received in revised form 27 November 2023

over a prolonged period of time (Vo et al., 2023). As such, they exhibit degradation because of the interplay between various mechanisms including plastic deformation and fracture (Vasileiou et al., 2021).

Material creep deformation is characterised by the strain rate, which dominates the overall response (Xiong et al., 2021). The creep strain rate is typically described using a modified Arrhenius power law (Bieberdorf et al., 2021; Xiong et al., 2022). For temperatures of 550 °C, components made from austenitic stainless steel such as 316H grade are expected to exhibit inelastic time dependent deformation through dislocation creep (Zauter et al., 1994). This process occurs through the glide of dislocations through a poly-crystalline material to cause deformation of individual grains when the applied stress is in the range 10–200 MPa (Petkov and Cocks, 2020), which is below the yield stress for an austenitic stainless steel, ie 205 MPa for 316H stainless steel.

Ductile fracture in metals typically occurs through the nucleation, growth, and the intergranular interlinking of voids (Gurson, 1977). Similarly, creep cavity initiation is seen at grain boundaries during creep (Sandström and He, 2022), and the average growth rate can be estimated using the macroscopic stress (Cocks and Ashby, 1982), while the final rupture is in the nature of a intergranular process. Lenticular cavities have been observed during creep at the grain boundaries in both 304 and 316 stainless steels, induced by a combination of high temperature void diffusion and dislocation climb (Chen and Argon, 1981; Morris and Harries, 1977). Factors including the temperature, local stresses and accumulated local strain are typically thought to contribute most to creep cavity nucleation and growth, but many of these mechanisms are accommodated and strongly influenced by the effect of the microstructure, such as grain orientations and carbide precipitates (Mianroodi et al., 2022; Hu et al., 2022; Duarte and Koslowski, 2023; Skamniotis et al., 2023). At high stress, both plastic deformation and creep take place, with plastic strain induced void initiation dominating the formation of damage. Although creep cavities can form in these conditions at grain boundaries, overall failure occurs due to ductile failure resulting from creep cavities and other features found at grain boundaries.

Understanding the deformation mechanisms at the grain length-scale that contribute towards the nucleation of voids and creep cavities that can lead to ductile failure is key to understanding fracture behaviour (Li et al., 2023). It is known through measurements performed with electron microscopy techniques that cavitation is more pronounced in boundaries with second phases and precipitates than in higher purity materials as observed in high purity aluminium by Yavari and Langdon (1983). Hard second phases such as martensite as well as $M_{23}C_6$ carbide precipitates containing elements such as chromium and molybdenum between 1 nm and 5 nm diameter can increase cavity nucleation (Sawada et al., 2019). Carbides more readily precipitate in samples aged at higher temperatures, accumulate in higher concentrations at grain boundaries, and influence plastic deformation (Agius et al., 2022). Certain grain boundary orientations will lead to higher levels of precipitation and carbide density (Hong et al., 2001; Jones et al., 2008), and are thought to cavitate earlier (Asqardoust et al., 2023; Yalçinkaya et al., 2021; Slater et al., 2017; He et al., 2021). However, carbide precipitates are too small in size to be explicitly modelled using micron scale crystal plasticity simulations.

The misorientation between neighbouring grains is also a key factor in fracture nucleation. The effect of the Taylor factor, which quantifies the average orientation and size of grains on fracture nucleation, has been investigated in ferritic steel (Tasan et al., 2014). It was found that damage tends to nucleate at the interface between high and low deformation zones, constituted of smaller grains and martensitic regions. Intergranular fracture in 316L stainless steel has been observed at the shorter grain boundaries between sets of elongated columnar grains, showing that grain morphology and length-scale effects also play an important role (Williams et al., 2021). Moreover, the effect of strain incompatibility measures, such as the density of geometrically necessary dislocations (GND), on fracture nucleation is not widely studied (Irastorza-Landa et al., 2017a). The effects of grain misorientation and carbides on fracture are intimately related because the grain boundary misorientation angle partly determines the carbide density. This in turn decreases the grain boundary critical energy release rate, as well as affecting the strain incompatibility and the local stress state during load. The combined effect of these two intrinsic mechanisms cannot be easily studied without a combined computational and experimental study. The effect that $M_{23}C_6$ carbides have on local strain fields has been studied in 420 stainless steel using crystal plasticity (Hidalgo et al., 2020).

Microscale modelling is an invaluable tool to characterise the plastic deformation and fracture at the length-scale of the individual grains (van der Giessen et al., 2020). The crystal plasticity finite element method (CPFEM) is an example of a modelling tool capable of reproducing phenomena relating to the incompatibility of the plastic deformation near the interface of grain pairs on the micron length scale (Roters et al., 2019), while dislocation-based constitutive laws can reproduce the effect of slip gradients on the local slip resistance (Zhang et al., 2023; Das et al., 2018). A number of studies discuss the coupling between the phase-field method and crystal plasticity with respect to the implementation of crystal plasticity approaches within the diffuse interface region, which is modelled by an order parameter in the context of the phase-field method (Abrivard et al., 2012; Ask et al., 2019; Prahs et al., 2023; Ali et al., 2023). In contrast, phase field fracture (PFF) models for single phase materials consider the phase field to describe the phase transition between undamaged and damaged materials. In PFF models, the field value varies between 0 for undamaged material, to 1 for completely damaged material. Within heterogeneous multi-phase materials, multiple crack order parameters have been utilised to reproduce fracture behaviour more accurately, such as that of Schöller et al. (2022). This approach has been applied to both brittle and ductile fracture at varying length-scales from component level simulations with continuum finite element approaches (Li et al., 2022a; Isfandbod and Martínez-Pañeda, 2021), to crystal plasticity mesoscale damage modelling of grain microstructures (Li et al., 2022b; Diehl et al., 2017; Flint et al., 2019).

The identification and description of influencing factors on damage initiation on the microstructural scale remains an open problem within the literature. Micro-structural modelling and simulation techniques have been applied to understand influencing factors in fatigue crack initiation, with crack initiation attributed to accumulated local plastic deformation and inclusions (Lu et al., 2016; Sistaninia and Niffenegger, 2014). The use of microscopy techniques has been used to identify damage features (He et al., 2023; Lian et al., 2014), however, a comprehensive approach encompassing the interplay between microstructural features, plastic strain localisation, and precipitates and second phases has been developed thus far. The effect of evolving microstructural texture under cyclic loading conditions has also been explored (Ragab et al., 2023).

Borden et al. developed a model incorporating a degradation function to account for plastic softening after crack initiation (Borden et al., 2016), a feature of particular interest when applied to microstructural modelling, due to the effect local damage can have on surrounding regions and grains. To better correlate with experimental results, many approaches, including a set of threshold conditions to prevent damage nucleation before high elastic or plastic deformation, have been attempted. Energy based damage criterion have been implemented utilising an additive split of elastic and plastic strain energy by Amor et al. (2009). These include thresholds in energy and strain like that of Miehe et al. (2015a), or plastic work thresholds implemented by Borden et al. (2016), in which a threshold is applied to control the point at which plastic deformation can contribute to failure initiation. PFF has been used for both crack nucleation and propagation, reproducing stress, transition flaw size and toughness criteria for fracture (Kristensen et al., 2021; Kumar et al., 2020). Although phenomenological from the modelling perspective, the introduction of thresholds and specific strain-based contributions to the fracture driving force has been used in many cases to more accurately capture nuanced, condition dependent behaviour observed in experiments and in-service material samples (Dittmann et al., 2020). Other fracture models, such as the cohesive zone model (Grilli et al., 2022a, 2021b), element elimination (Grilli et al., 2022b) and Beremin model (Forget et al., 2016) can be used to predict damage formation surrounding micro-structural defects such as carbide precipitates. However, in the present work, PFF is used because of the large area analysed, the capability of modelling localised damage within a microstructure, and the ability to use a structured mesh. The localisation of the crack surface is a key feature of PFF that allows to model creep fracture in materials like 316H stainless steel, in which cracks localise at the grain boundary.

Despite the increasing popularity of using phase field damage models to approach the problem of crack nucleation and propagation, Gurson-Tvergaard-Needleman (GTN) models have been well studied within the literature for analysing the nucleation, growth, and coalescence of voids for ductile failure (Zhang et al., 2000). The novelty in the approach presented within this work is two-fold. Firstly, the demonstration of capturing localised damage initiation within a material microstructure and estimating the void volume fraction by comparison to the magnitude of the phase field through links to microstructural morphology. Secondly, the capturing of microstructural damage initiation within a modelling framework that can also model crack path propagation.

The following scientific questions remain unanswered: how much damage is induced by plastic and creep deformation respectively in 316H stainless steel depending on the applied stress? What is the interplay between grain boundary misorientation and carbides, and how can their effect on damage initiation be quantified? How much does the grain boundary critical energy release rate decrease in the presence of a specific carbide density or grain boundary orientation? Which is the most accurate indicator of damage across a microstructural region, in terms of dislocation density, elastic strain energy, or plastic work done? Are microstructural models for plasticity and fracture capable of predicting the cavity nucleation on individual grain boundaries? How effectively can continuous phase field models in conjunction with crystal plasticity, which have previously been mostly used in modelling crack propagation, be applied to early damage formation? In this article, a combination of coupled crystal plasticity-fracture simulations and electron microscopy experiments are used to consider and address these questions, in order to present a comprehensive model that accounts for the combined effect of grain misorientations and intergranular carbides reducing the local fracture energy at grain boundaries. Understanding the interplay between different mechanisms at the micro-scale in the formation and propagation of damage resulting from deformation is a key focus (Abdolvand, 2022), particularly in experimental specimens observed by He et al. (2023), and the modelling work shown here.

Electron microscopy techniques such as scanning electron microscopy (SEM) and electron backscatter diffraction (EBSD) allow for imaging and grain microstructure characterisation at up to nanometre resolution. The high resolution of SEM allows for voids, cavities, and other features of damage formation to be resolved and identified (Chen et al., 2011). EBSD measurements allow for the orientations of grains to be determined which when combined and correlated with identified voids and damage features allow for significant insight into the underlying mechanisms of damage formation, as done by He et al. (2021), Martin et al. (2020), He et al. (2023). The combination of high throughput microscope detectors and interrupted mechanical tests allows damage nucleation over large areas, with the size of several square millimetres, to be investigated (You et al., 2023; Martin et al., 2022; He et al., 2023).

This article is organised as follows. Section 2 explains the computational method, including the crystal plasticity finite element method (CPFEM) framework in Section 2.1 and the phase field fracture (PFF) formulation in Section 2.2. Section 3 contains the experimental characterisation of the 316H stainless steel sample, with 4 and 5 detailing how the simulation parameters were calibrated and analysed. The final results are outlined in Section 6, which is split into Section 6.1, 6.3, 6.2, and 6.4 to detail results and analysis from the various crystal plasticity phase field models that have been implemented including the reference elastic strain energy damage model, a misorientation dependent critical energy release rate, an elastoplastic damage model, and a plastic-creep deformation crystal plasticity model respectively. Results are discussed and evaluated in the context of the outlined objectives and questions in Section 7, with concluding statements in Section 8, and a supplementary appendix in Appendix.

2. Computational method

In this section, the coupled CPFE-PFF methodology used in the simulations is presented. The computational method solves for the three components of the displacement vector $\boldsymbol{u}$ and for the scalar damage phase field variable c. The Cauchy stress tensor $\boldsymbol{\sigma}$ is calculated from the deformation gradient $\boldsymbol{F}$, as described in Section 2.1. The local form of the quasi-static equilibrium problem neglecting body forces reads:

$$\nabla \cdot \boldsymbol{\sigma} = 0 \, , \tag{1}$$

is solved, together with the evolution equation for the damage phase field, as detailed in Section 2.2. The model is implemented in the MOOSE multiphysics finite element framework (Permann et al., 2020) through a Fortran-based UMAT material subroutine.

Table 1
Elastic constants used as cubic elasticity parameters in FCC 316H stainless steel.

Elastic constant	Value	Units
C_{11}	204.6	GPa
C_{12}	137.7	GPa
C_{44}	126.2	GPa

2.1. Crystal plasticity formulation

A CPFE model, based on the integration scheme originally proposed by Kalidindi et al. (1992), is employed. The total deformation gradient can be decomposed into elastic and plastic components, denoted $\boldsymbol{F}_e$, and $\boldsymbol{F}_p$ respectively, as shown below (Asaro and Rice, 1977; Kalidindi, 1998):

$$\boldsymbol{F} = \boldsymbol{F}_e \boldsymbol{F}_p \ . \tag{2}$$

Simulations are conducted at constant temperature, 550 °C, which is the same used in the experiment, and the model parameters reflect the material properties at that temperature. Therefore, no thermal expansion mechanism is included in this model. $\boldsymbol{F}_p$ represents the plastic component of the deformation gradient, accounting for the plastic deformation contributions across all available slip systems in the crystal structure. The time evolution of $\boldsymbol{F}_p$ is described by Grilli et al. (2018b):

$$\boldsymbol{L}_p = \dot{\boldsymbol{F}}_p \boldsymbol{F}_p^{-1} = \sum_{\alpha=1}^{N_s} \dot{\gamma}^\alpha \boldsymbol{s}^\alpha \otimes \boldsymbol{n}^\alpha \ , \tag{3}$$

where $\boldsymbol{L}_p$ is the plastic velocity gradient, α is the index characterising each slip system, whose unit vector for the slip direction is $\boldsymbol{s}^\alpha$ and slip plane normal is $\boldsymbol{n}^\alpha$ at the intermediate configuration. The slip rate of each slip system is represented by $\dot{\gamma}^\alpha$, which includes two contributions: plastic slip and creep. The number of slip systems in the crystal structure is given by $N_s = 12$ because 316H stainless steel consists of a dominant austenite phase with a face centred cubic (FCC) structure.

The model implementation is performed in a large strain framework which has been designed for general use, which can be applied to small strain problems. The small strain modelling application is in small strains as the experimental application was also using small strains. A cubic elasticity matrix for face centred cubic (FCC) structure materials was used, the 6 × 6 Mandel notation form of which is shown below:

$$\underline{\underline{C}} = \begin{bmatrix} C_{11} & C_{12} & C_{12} & 0 & 0 & 0 \\ C_{12} & C_{11} & C_{12} & 0 & 0 & 0 \\ C_{12} & C_{12} & C_{11} & 0 & 0 & 0 \\ 0 & 0 & 0 & C_{44} & 0 & 0 \\ 0 & 0 & 0 & 0 & C_{44} & 0 \\ 0 & 0 & 0 & 0 & 0 & C_{44} \end{bmatrix} . \tag{4}$$

The values of the cubic elastic constants used for 316H stainless steel are shown below in Table 1:

Two power law terms, as proposed by Rice (1971), are used to calculate the plastic strain rate due to plastic slip and creep respectively:

$$\dot{\gamma}^\alpha = \dot{\gamma}_0^s \left(\frac{|\tau^\alpha|}{\tau_c^\alpha} \right)^{1/m_s} \mathrm{sign}\,(\tau^\alpha) + \dot{\gamma}_0^c \left(\frac{|\tau^\alpha|}{\tau_c^\alpha} \right)^{1/m_c} \mathrm{sign}\,(\tau^\alpha) \ , \tag{5}$$

where $\dot{\gamma}_0^s$ and $\dot{\gamma}_0^c$ are constant strain rate prefactors, m_s and m_c are constant exponents for the plastic slip and creep respectively, which are the same for each slip system. The conditions for the experimental sample consisted of an initial load-up phase followed by a long creep phase. These parameters are chosen in such a way to simulate the conditions of the experimental sample, in which the plastic slip term dominates during the initial load-up phase to 0.14% strain. The creep deformation term then dominates for the subsequent creep phase, as detailed in Section 4. τ^α is the resolved shear stress (RSS) in each slip system α, while the critical resolved shear stress (CRSS), τ_c^α, is given by Bayley et al. (2006), Franciosi and Zaoui (1982), Grilli (2016):

$$\tau_c^\alpha = \tau_c^0 + \alpha_0 \mu b \sqrt{\sum_{\beta=1}^{N_s} \chi_\beta^\alpha \left(\rho_{\mathrm{SSD}}^\beta + \left| \rho_{\mathrm{eGND}}^\beta \right| + \left| \rho_{\mathrm{sGND}}^\beta \right| \right)} \ , \tag{6}$$

where τ_c^0 is a constant Peierls stress, needed to move a dislocation within a plane of atoms, α_0 is the Taylor hardening prefactor, μ is the shear modulus, b the Burgers vector length. Each slip system is characterised by three state variables quantifying the dislocation density, these are: $\rho_{\mathrm{SSD}}^\alpha$, the statistically stored dislocation (SSD) density, $\rho_{\mathrm{eGND}}^\alpha$ and $\rho_{\mathrm{sGND}}^\alpha$, the density of geometrically necessary dislocations (GND) with edge and screw character respectively. This model choice is important to quantify the effect of slip gradients and of the grain size and morphology on the stress state. This is necessary because the stress state near grain boundaries determines intergranular fracture nucleation due to void formation (Grilli et al., 2021a). χ_β^α is the latent hardening matrix that describes the interaction hardening effect induced by the slip system β on the slip system α. In FCC crystals, this is described using a symmetric

Table 2
Slip interactions coefficients used FCC crystal structured 316H stainless steel (Arsenlis and Parks, 2002) .

Type	Self-interaction	Co-planar	Cross-slip	Glissile	Hirth lock	Lomer-Cottrell lock
χ^α_β	0.1	0.22	0.3	0.38	0.16	0.45

12 × 12 matrix whose entries represent different types of interactions between the slip systems, such as self-interaction, co-planar, cross-slip, glissile dislocations, Hirth and Lomer-Cottrell locks. The specific form of the matrix is reported in Franciosi and Zaoui (1982), while the values of χ^α_β for the different types of interactions in 316H are given in Table 2, reported by Arsenlis and Parks (2002).

The evolution law for the SSD density $\rho^\alpha_{\mathrm{SSD}}$ includes the dislocation multiplication and annihilation (Grilli et al., 2015; Hu et al., 2023):

$$\dot{\rho}^\alpha_{\mathrm{SSD}} = \left(k_m \sqrt{\rho^\alpha_{\mathrm{SSD}} + \left|\rho^\alpha_{\mathrm{eGND}}\right| + \left|\rho^\alpha_{\mathrm{sGND}}\right|} - 2 y_c \rho^\alpha_{\mathrm{SSD}} \right) \frac{\left|\dot{\gamma}^\alpha\right|}{b} \, , \tag{7}$$

where k_m is the accumulation rate, y_c is the critical annihilation distance for adjacent dislocations, which has been measured accurately for 316 stainless steel (Catalao et al., 2005). The evolution law for ρ^α_{SSD} can reproduce hardening and saturation in FCC metals and the parameters will be calibrated by comparing the simulation results with experimental stress–strain curves. The evolution of the GND density is calculated using slip gradient (Yalçinkaya et al., 2021), specifically their projections along the slip direction, $\boldsymbol{s}^\alpha$ and along the edge dislocation line direction, $\mathbf{t}^\alpha$ (Ashby, 1970):

$$\dot{\rho}^\alpha_{\mathrm{eGND}} = -\frac{1}{b} \nabla \dot{\gamma}^\alpha \cdot \mathbf{s}^\alpha \, , \tag{8}$$

$$\dot{\rho}^\alpha_{\mathrm{sGND}} = -\frac{1}{b} \nabla \dot{\gamma}^\alpha \cdot \mathbf{t}^\alpha \, . \tag{9}$$

These relationships incorporate a length-scale dependence of the CRSS in the model, which is essential to capture the stress state near grain boundaries (Pai et al., 2022). The edge dislocation line direction, which is equivalent to the direction of motion of positive screw dislocations is calculated as:

$$\boldsymbol{t}^\alpha = \boldsymbol{s}^\alpha \times \boldsymbol{n}^\alpha \, . \tag{10}$$

The relationships (8) and (9) are calculated numerically by representing $\dot{\gamma}^\alpha$ with linear shape functions. The specific interpolation in each element is carried out by using the numerical values of $\dot{\gamma}^\alpha$ calculated from (5) at the integration points. In this section, the evolution laws of the plastic deformation gradient as a function of the stress state have been presented, while in the next section, the damage model, together with the stress calculation, will be shown. The equations of the CPFE model have been implemented into a UMAT subroutine, which can be utilised with different solvers.

2.2. Phase field damage formulation

The phase field damage model is coupled with the crystal plasticity formulation in Section 2.1 to describe damage nucleation and propagation during both plastic and creep deformation. It is based on a continuum damage variable c that can take any value between 0 and 1 (Grilli and Koslowski, 2019; Grilli et al., 2017). Here, c indicates the damage level of the material where a value of 0 indicates undamaged material and 1 indicates entirely damaged material. This model is based on a free energy formulation, in which the free energy per unit volume, Ψ, includes the mechanical part Ψ_m and the energy released by fracture surfaces Ψ_f,

$$\Psi = \Psi_f + \Psi_m \tag{11}$$

which is regularised as an integral over the volume of the domain Ω (Grilli and Koslowski, 2018):

$$\Psi_f = \int_\Omega G_c \gamma(c, \nabla c) \, dV = \int_\Omega \frac{G_c}{2} \left(\frac{c^2}{l_0} + l_0 \left|\nabla c\right|^2 \right) dV \, , \tag{12}$$

where G_c is the critical energy release rate for fracture defined in Griffith's theory (Griffith and Taylor, 1921), $\gamma(c, \nabla c)$ is the regularised crack energy functional and l_0 is the characteristic regularisation length-scale, dictating the diffusiveness of the damage field. To incorporate the twist and tilt of a grain boundary, characterised by a misorientation angle $\Delta\theta$, G_c is set as a function of the coordinates. Specifically, it depends on the misorientation between neighbouring grains $\Delta\theta$ near a grain boundary, while it has a constant value in the inner part of grains, as detailed in Section 2.4. The mechanical free energy Ψ_m is decomposed into a part that drives the damage evolution, a^+, and a part that is not affected by damage, a^-:

$$\Psi_m = \int_\Omega a \, dV = \int_\Omega \left[(1-c)^2 + k_r \right] a^+ \, dV + \int_\Omega a^- \, dV \, , \tag{13}$$

where k_r is a small residual stiffness, which is necessary for convergence when parts of the representative volume are completely damaged. $a^+\left(\boldsymbol{F}_e\right)$ and $a^-\left(\boldsymbol{F}_e\right)$ are functions of the elastic deformation gradient $\boldsymbol{F}_e$. A dissipation function $\mathscr{D}$ is introduced, which represents the plastic work rate $\dot{W}_p$, whose form follows that of Ziegler (1983), Lee (1969):

$$\mathscr{D}\left(\boldsymbol{F}_e, \boldsymbol{F}_p, \dot{\boldsymbol{F}}_p\right) = \dot{W}_p = \int_V \mathrm{tr}(\boldsymbol{\sigma} \boldsymbol{F}_e \dot{\boldsymbol{F}}_p \boldsymbol{F}_p^{-1} \boldsymbol{F}_e^{-1}) \det(\boldsymbol{F}_e) \, dV \, . \tag{14}$$

For the monotonic loads used in the present work, W_p is the total plastic work done, a monotonically increasing function. Since in a finite strain anisotropic medium the elastic energy cannot be decomposed into a part given by the volumetric strain only and a part given by the isochoric strain only (Lee, 1969), an effective bulk modulus K will be used in the following:

$$K = \frac{1}{9}\sum_{i,j=1}^{3} C_{iijj} \ , \tag{15}$$

where C_{ijkl} denote the individual components of the fourth-order stiffness tensor, $\mathbb{C}$. This property derives from the multiplicative, and not summative, decomposition of the elastic and plastic deformation gradient in a finite strain formalism. Since the time derivative of the energy per unit volume is given by the product between the Cauchy stress and the velocity gradient, a summative decomposition would not be possible. The part of the mechanical Helmholtz free energy that drives damage is decomposed as follows:

$$a^{+} = a^{+}_{\mathrm{cpl}} + a^{+}_{\mathrm{vol}} \ , \tag{16}$$

where a^{+}_{vol} is the positive volumetric free energy, a^{+}_{cpl} is the coupled free energy, which is defined as the difference between the total mechanical free energy of the anisotropic medium and the volumetric part of an equivalent isotropic linear elastic material with bulk modulus K. The part of the mechanical Helmholtz free energy that is not affected by damage is equivalent to the negative volumetric free energy:

$$a^{-} = a^{-}_{\mathrm{vol}} \ , \tag{17}$$

which represents the fact that, typically, volumetric compression does not induce damage in metals. By substituting Eqs. (17), (16), (13), and (12) into equation (11), the full description of the free energy is found and shown below:

$$\Psi = \int_{\Omega} \frac{G_c}{2}\left(\frac{c^2}{l_0} + l_0\left|\nabla c\right|^2\right) dV + \int_{\Omega} \left[(1-c)^2 + k_r\right](a^{+}_{vol} + a^{+}_{cpl})\, dV + \int_{\Omega} a^{-}_{vol}\, dV \ , \tag{18}$$

The dissipation function in (14) depends on the damage phase field through the Cauchy stress $\boldsymbol{\sigma}$. The positive and negative volumetric free energies are calculated as:

$$a^{+}_{\mathrm{vol}} = \begin{cases} \frac{1}{2}K\omega^2 \ , & \text{if } J_e \geq 1 \ , \\ 0 \ , & \text{if } J_e < 1 \ , \end{cases} \tag{19}$$

$$a^{-}_{\mathrm{vol}} = \begin{cases} 0 \ , & \text{if } J_e \geq 1 \ , \\ \frac{1}{2}K\omega^2 \ , & \text{if } J_e < 1 \ , \end{cases} \tag{20}$$

where:

$$\omega = \frac{3}{2}\left(J_e^{2/3} - 1\right) \ , \tag{21}$$

is the elastic volumetric expansion. The coupled free energy is given by:

$$a^{+}_{\mathrm{cpl}} = \frac{1}{2}\boldsymbol{E}_e : \mathbb{C} : \boldsymbol{E}_e - \frac{1}{2}K\omega^2 \ , \tag{22}$$

where the Green–Lagrange elastic strain tensor, $\boldsymbol{E}_e$, is given by:

$$\boldsymbol{E}_e = \frac{1}{2}(\boldsymbol{F}_e^T\boldsymbol{F}_e - \boldsymbol{I}) = \frac{1}{2}\left(\boldsymbol{C}_e - \boldsymbol{I}\right) \ , \tag{23}$$

where $\boldsymbol{C}_e$ is the right elastic Cauchy–Green tensor and $\boldsymbol{I}$ is the identity matrix. The coupled free energy a_{cpl} corresponds to the free energy given by the deviatoric strain in the small strain formulation. Overall, the second Piola–Kirchhoff stress tensor $\boldsymbol{S}$ is derived by:

$$\boldsymbol{S} = \frac{\partial a}{\partial \boldsymbol{E}_e} = \begin{cases} \left[(1-c)^2 + k_r\right]\mathbb{C} : \boldsymbol{E}_e \ , & \text{if } J_e \geq 1 \ , \\ \left[(1-c)^2 + k_r\right]\left(\mathbb{C} : \boldsymbol{E}_e - J_e^{2/3}K\omega\boldsymbol{C}_e^{-1}\right) + J_e^{2/3}K\omega\boldsymbol{C}_e^{-1} \ , & \text{if } J_e < 1 \ . \end{cases} \tag{24}$$

Note that the dissipation function does not depend on the time derivative of $\boldsymbol{E}_e$, thus it does not contribute to the stress tensor (Ziegler, 1983). However, it depends on the damage phase field, hence the plastic work affects the time evolution of c. Note that the stress degradation under a tensile load represents a loss of stiffness, which can be interpreted as the presence of voids in the system. The evolution of c is determined by the minimisation of the sum of the free energies, Ψ_f, Ψ_m and of the dissipation function $\mathscr{D}$. However, in this work, a rate-dependent approach is adopted, based on an Allen-Cahn equation, which ensures the local growth of the fracture phase field (Miehe et al., 2010a, 2015b):

$$\dot{c} = \frac{1}{\eta}\left\langle l_0\Delta c - \frac{c}{l_0} + 2(1-c)\frac{\left(a^{+} + \beta W_p\right)}{G_c}\right\rangle \tag{25}$$

where η is a kinetic coefficient, and $\langle\rangle$ indicate McCauley brackets, where $\langle x\rangle = x$ if $x > 0$ and $\langle x\rangle = 0$ if $x < 0$. β is a prefactor of the plastic work contribution, taking values between 0 and 1. Even though, originally, the phase field fracture model was based on the elastic strain energy only (Grilli et al., 2018a; Duarte et al., 2018), a modification to include the plastic work into the damage evolution law is used in the present work. In the following, simulations are carried out with both $\beta = 0$ and $\beta = 1$; the comparison with experiments reveals the contribution of plastic work to local damage. Including the contribution to damage from both volumetric and isochoric strain is important for metals because the effect of stress triaxiality is required to characterise fracture nucleation in ductile materials (Borden et al., 2016). For instance, both terms are included to predict the yield strength and void volume fraction in models such as the Gurson-Tvergaard-Needleman (Hao and Brocks, 1997). The hypothesis that is being tested in this work is that the damage phase field c is representative of the void nucleation, as compared to experimental measurements of the void fraction.

2.3. Numerical implementation

Details of the algorithm used for determining the plastic deformation gradient and the stress at each time step is presented in Appendix A, in particular the Jacobian calculation that is required for the coupled plasticity-damage model, which has not been previously reported in the literature. The CPFE model is coupled with phase field fracture using the MOOSE multiphysics finite element framework (Permann et al., 2020). A monolithic solver is used for the stress equilibrium (1) and for the damage evolution (25), which is based on the preconditioned Jacobian-free Newton-Krylov method, which provides an increased computational efficiency (Chockalingam et al., 2013). Specifically, the hypre BoomerAMG algebraic multigrid solver has been chosen, both as a solver and as a preconditioner, because of its speed (Falgout and Yang, 2002).

2.4. Misorientation dependent critical energy release rate

To characterise the strength of different types of grain boundaries, the local critical energy release rate G_c is set as a function of the local misorientation angle $\Delta\theta$. This is defined in each element of the mesh as the maximum misorientation between the element and its neighbours. The scalar misorientation $\Delta\theta$ between two neighbouring points A and B, whose orientation is described by three dimensional crystal rotation matrices determined from Euler angles, $\mathbf{R}_{\mathrm{A}}$ and $\mathbf{R}_{\mathrm{B}}$, is determined based on the misorientation matrix $\Delta\mathbf{R}_{\mathrm{AB}} = \mathbf{R}_A^{-1}\mathbf{R}_B$, as detailed in Irastorza-Landa et al. (2017b). Specifically, the rotation matrices are calculated in each element by considering the Euler angles obtained from EBSD measurements. 432 FCC crystal symmetry operation matrices $\boldsymbol{G}_i$ (with $i = 1, \ldots, 24$) must be accounted, which are explicitly reported in Appendix B. This is because symmetry operations do not change the atomic arrangement in a grain, but they affect the misorientation calculation. Therefore, all possible combinations of symmetry operations are applied to the rotation matrices $\mathbf{R}_{\mathrm{A}}$ and $\mathbf{R}_{\mathrm{B}}$ before the scalar misorientation calculation is carried out; the minimum between all possible results is selected. Mathematically, $\Delta\theta$ can be defined as (Pantleon, 2008):

$$\Delta\theta = \min_{i,j}\left(\arccos\left(\frac{\mathrm{Tr}(\boldsymbol{G}_i^{-1}\mathbf{R}_A^{-1}\mathbf{R}_B\boldsymbol{G}_j) - 1}{2}\right)\right) \tag{26}$$

where i, j are pairs of indices with $i = 1, \ldots, 24$ and $j = 1, \ldots, 24$. This definition of scalar misorientation provides values in the interval from 0°to 62.8°. To understand the effect of the grain boundary carbides on grain boundary strength, different functions $G_c\,(\Delta\theta)$ are used in the simulations. The higher density of carbides observed in the microscopy experiments at $\Delta\theta = 27°$, as detailed in Section 6.2, has motivated the choice of trial functions $G_c\,(\Delta\theta)$ with a minimum value at that specific misorientation angle. Specifically, three different dependencies are used: linear, quadratic, and trapezoidal, as shown in Fig. 1(a). Simulations using these functions will be used to find the best agreement with the misorientation dependence of damage nucleation in the high temperature mechanical test. The minimum and maximum values of $G_c\,(\Delta\theta)$ will be calibrated by comparing with the measured cavitation ratio during the experiment. Thus, the reduction of the grain boundary critical energy release rate due to the carbides can be determined. The interval of $(\Delta\theta)$ in Fig. 1(a) starts from 10° because that is the smallest misorientation observed among the grain boundaries in the analysed polycrystal. An example of G_c as a function of the position in the analysed polycrystal structure is shown in Fig. 1(b), where the blue regions correspond to the grain boundaries with the lowest critical energy release rate.

The variation in the critical energy release rate is applied on an element by element basis. Since the misorientation angle is only calculated for two elements either side of a grain boundary, only these elements have the modified value of G_c. The characteristic length-scale of the phase field model was approximately half the element size at 3 μm.

3. Experimental characterisation

He et al. (2023) have recently investigated the use of correlative microstructural characterisation in creep cavitation in 316H stainless steel, but a systematic comparison with microstructural simulations was not carried out. The material studied was extracted from an ex-service boiler header made of type 316H austenitic stainless steel, whose chemical composition is given in Table 3. The component was provided by EDF Energy Ltd. and it was first operated at a temperature between 490 °C and 530 °C for 65000 h in a steam header.

Electron microscopy characterisation of a 316H stainless steel sample after high temperature deformation was carried out, the aim of which was to test the CPFE model to understand the contributions of different mechanisms to damage nucleation. A key component of this was to conduct direct comparisons to experimental samples over the same microstructure to identify which regions of high damage can be explained by certain mechanisms.

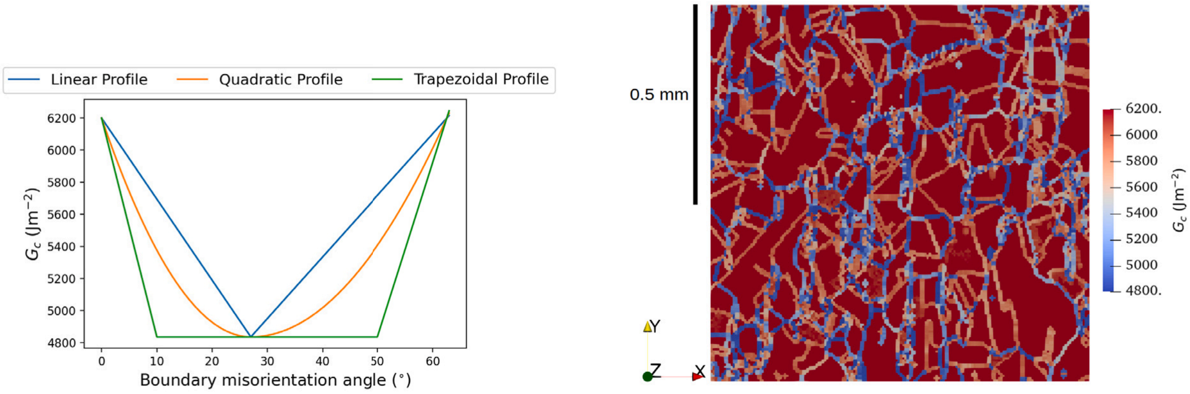

(a) (b)

Fig. 1. (a) Local critical energy release rate G_c as a function of the misorientation angle $\Delta\theta$ for the three analysed profiles. (b) The variation in G_c across differently oriented boundaries in the analysed polycrystalline structure for the trapezoidal profile. (For interpretation of the references to colour in this figure legend, the reader is referred to the web version of this article.)

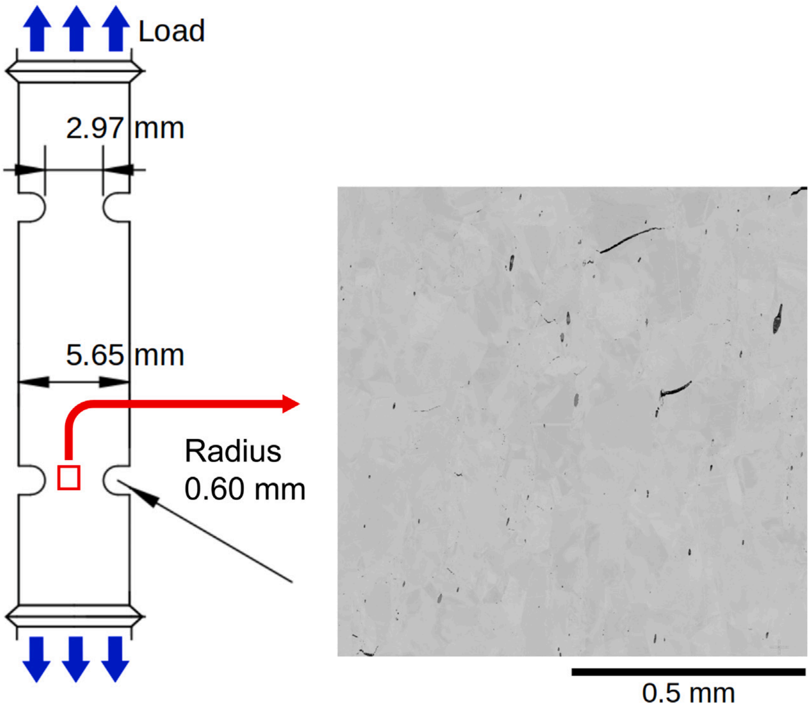

(a) (b)

Fig. 2. (a) Notched specimen and (b) An SEM image of the area of interest for the cavitation measurement; black spots indicate damaged regions.

A uniaxial high temperature specimen with a double notch, each of 0.60 mm radius, and a notch diameter to notch root ratio of 10 was used. The longitudinal section is shown in Fig. 2(a). The sample was mechanically tested under strain control: first, the strain is increased linearly, until a far field stress value of 390 MPa is reached, leading to plastic deformation near the notch; second, stress relaxation due to creep deformation take place at constant strain for 500 h; third, the strain is increased until 390 MPa is reached again. This procedure is repeated 25 times; thus the total dwell time is 25 × 500 h.

The tested specimen was cut axially across the centre of the notch for correlative microstructural characterisation. Correlative Electron Backscatter Diffraction (EBSD) and Scanning Electron Microscopy (SEM) microstructural characterisation was performed by scanning across the notch section with both techniques and correlated in spatial coordinates through post image processing. A

Table 3
The nominal composition of the ex-service 316H stainless steel header material (mass %).

C	Si	Mn	P	S	Cr	Mo	Ni	B	Co	Fe
0.060	0.400	1.980	0.021	0.014	17.170	2.190	11.830	0.005	0.100	66.230

Zeiss SigmaHD FEG-SEM equipped with a DigiView 3 EBSD detector was used for the EBSD and SEM characterisation. The EBSD data was obtained at a voltage of 25 kV and a step size of 3 μm, while the SEM at 20 kV voltage. The image segmentation software Dragonfly (Object Research Systems [ORS] Inc., Canada) was then applied to segment creep cavities from the SEM image. The segmentation was performed with a deep-learning platform in the Dragonfly software which was trained with randomly selected SEM frames, followed by manual work to reduce errors of automatic segmentation. The EBSD data in this study was processed by MTEX toolbox (Hielscher and Schaeben, 2008), where grain boundaries were calculated. In-house MATLAB scripts were written to project the segmented creep cavity data from Dragonfly onto the grain boundary data from EBSD, using fiducial marks inserted onto the specimen every 1 mm by focused ion beam (FIB) to calibrate the images. The combined cavity and grain orientation data has been used to study correlations between local microstructure and damage initiation (Martin et al., 2022). The competing processes acting for damage formation in such specimens will be plastic void initiation as well as creep cavitation. Due to the stress induced of 390 MPa being well above the yield stress of the material at 550 °C, it is posited that plastic void initiation and growth is the dominant mechanism acting.

4. Simulation setup and model calibration

4.1. Material parameters

Fig. 3 shows the simulated stress strain response and simulated stress–strain curves. Standard values were obtained from the literature for the elastic constants of 316H stainless steel (Agius et al., 2022). The calibrated material parameters are shown in Table 4. Values for parameters such as the accumulation rate coefficient k_m, the initial SSD density, ρ_{SSD}, and the dislocation capture radius, y_c, were obtained using a scipy.optimise in-house tool, called PyDakota (Grilli and Salvini, 2022). Initially, the residual between an output stress strain curve taken from the CPFE model and a stress strain curve on the same material at the same temperature was calculated. A non-gradient based Nelder–Mead algorithm was used to determine the next generation values of k_m, ρ_{SSD}, and y_c. This process was repeated until an agreement threshold condition for the residual between the curves from the experiment and the CPFE model was met. The Nelder–Mead algorithm is a non-local method meaning that the algorithm did not search the entirety of the parameter input space for the optimum set of inputs. This resulted in finding local minima in the residual between the model and experimental inputs, suggesting that alternative sets of input parameters could have reproduced the same stress strain response. Additionally, the process is sensitive to the initial starting point, which resulted in obtaining solutions corresponding to different local minima. In order for the calibration process used here to be considered valid, it was ensured that any calibrated parameters had values that made physical sense to ensure that the crystal plasticity model response were considered to have a physical interpretation and basis.

For the combined creep plasticity deformation model, the plastic slip term in Eq. (5) is included whilst the sample is initially loaded. After this, only the creep deformation term is active from then until the matching experimental time has elapsed. This allows the simulation to better match the experimental conditions which consisted of an initial tensile straining before a lengthy dwell time at constant load. Input parameter calibration for the creep deformation term in Eq. (5) was done through the same iterative process as for other crystal plasticity input by comparison to reference experimental specimen data. The calibrated value of the annihilation length ensured that the model maintains the saturation behaviour of dislocation densities after linear hardening. The parameter calibration is suitable since the range over which the stress strain curve for input parameters lay within the same stress range as that of the experimental specimen.

4.2. Material critical energy release rate calibration

G_c is the critical energy release rate of the material used in the phase field model. It describes the threshold energy that the Helmholtz free energy must exceed locally for the phase field to rapidly evolve at that point. It dictates both the early evolution behaviour of damage initiation as well as the final strain to fail when subjected to tensile conditions. Using an engineering strain to failure value of 35%, similar to those observed in the literature (Mehmanparast et al., 2013), a set of simulations were used with varying values of G_c over a sample section of the EBSD microstructure to the point of failure. A plot relating the strain for failure of the simulated material against the initial value of G_c was used to determine an appropriate value of G_c that would result in the expected strain to fail in the model.

From the graph shown in Fig. 3, the initial value of G_c was determined using the phase field model based on the elastic strain energy to damage to be 6200 J m^{-2}. A similar procedure was followed with the amended phase field model containing a formulation to include both the elastic and plastic strain energy and G_c was determined to have a value of approximately 10500 J m^{-2}. The EBSD microstructure consisted of 59 elements measuring 300 μm in the X direction and 19 elements measuring 100 μm in the Y direction. The grain microstructure displaying the phase field value once crack propagation was achieved is shown within the bottom right of Fig. 3(b) It has a sufficient number of grains and size length to be indicative of overall failure due to how rapidly crack propagation

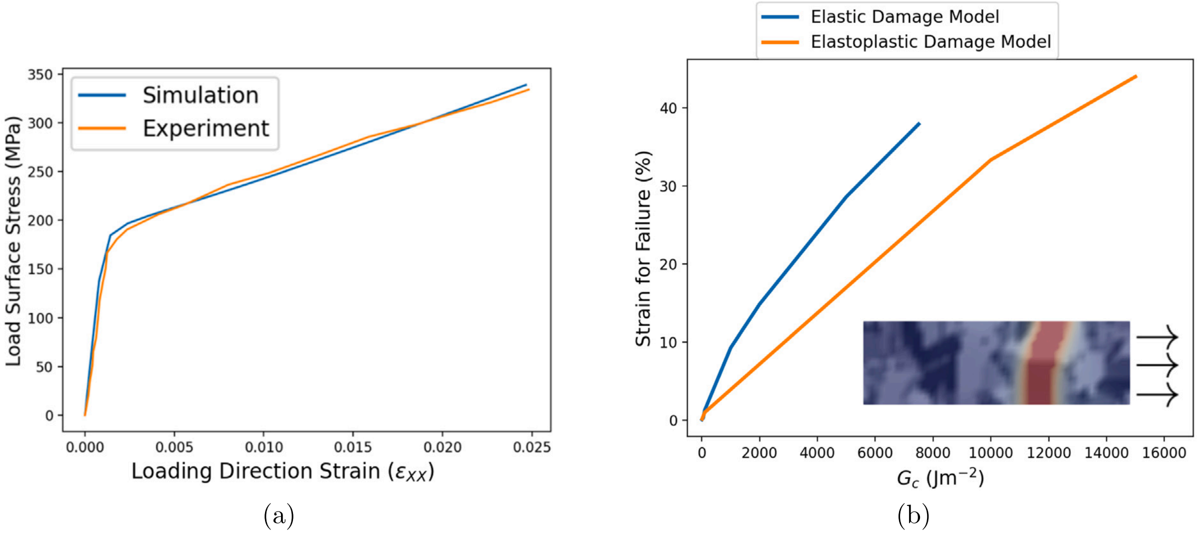

Fig. 3. (a) The Cauchy stress in the loading direction averaged over the load surface plotted against the total Green–Lagrange strain in the loading direction for the calibrated crystal plasticity model for 316H stainless steel under uniaxial tension at 550 °C with the literature data used for calibration using a scipy.optimise procedure (Petkov et al., 2019). (b) Calibration of the critical energy release rate using the strain to failure. The value of G_c determined for the reference elastic strain energy damage model was 6200 J m^{-2}. For the elastoplastic damage model, the value of G_c determined was 10500 J m^{-2}. The bottom left displays the output microstructure at failure, with red showing the crack path defined by the phase field and black showing the underlying grain microstructure. (For interpretation of the references to colour in this figure legend, the reader is referred to the web version of this article.)

progresses once the process starts. The phase field is represented by red within the inset, with the underlying grain microstructure shown in black. The width of the crack as it appears in the inset of Fig. 3b results from the colorbar selection. The width of the crack is narrower than the figure can be interpreted as showing. Choices for colorbars are chosen in order to clearly delineate the difference between the microstructure and the phase field.

5. Simulation analysis procedure

The simulation output data visualisation and analysis was done using a combination of ParaView and Python. An algorithm was designed to determine whether any element lay on a boundary to analyse the initiation of grain boundary damage. Each element orientation was compared to that of the adjacent elements. If any of the orientation Euler angles differed by a misorientation angle of more than ten degrees both the element and the adjacent were logged. Specific element data could then be picked out and analysed. A series of microstructural factors were investigated. Firstly, He et al. (2023), found little correlation between boundary Schmid factor difference and average boundary Schmid factor with grain boundary damage. The Schmid factor, m, of each slip system, α, for each grain was calculated using the rotation matrix $\boldsymbol{R}$, based on Euler angle orientations and the slip plane normals and directions, $\boldsymbol{n}_\alpha$ and $\boldsymbol{s}_\alpha$ respectively, as well as the loading direction, $\boldsymbol{q}$:

$$m_\alpha = (\boldsymbol{R}\ \boldsymbol{s}_\alpha \cdot \boldsymbol{q})(\boldsymbol{R}\ \boldsymbol{n}_\alpha \cdot \boldsymbol{q})\ . \tag{27}$$

The slip system resulting in the greatest value of m for a particular grain orientation was used moving forward to calculate the arithmetic mean Schmid factor across a grain boundary and the difference in Schmid factor across a grain boundary. It should be noted that the Schmid factor does not necessarily indicate which specific slip system is primarily active. For example, this can occur in the presence of obstructions such as second phases, inclusions, precipitates, or other obstructions to slip.

Secondly, a question to be addressed by the analysis here was to determine the magnitude of the influence of grain boundary misorientations on the formation of intergranular damage within a structure. The grain misorientation angle as determined by the relative orientations of two adjacent grains and the underlying crystal structure of both grains was calculated using the methodology described in Section 2.4.

There is no accepted standard within the literature on how to draw a correlation between a continuous damage variable such as a phase field in the case of damage initiation for cavity and plasticity induced void formation. For the purposes of this work, a threshold damage value, c_0, was determined relative to the maximum damage observed within the microstructure for a given simulation, $c_{\max}$ using a threshold prefactor, λ, which could take a value between 0 and 1.

$$c_o = \lambda \cdot c_{\max} \tag{28}$$

If a grain boundary element, i, had a phase field damage value, c_i greater than or equal to this threshold $c_0 = \lambda \cdot c_{\max}$, then cavitation was said to have occurred. Therefore, the cavitation condition is $c_i \geq c_o$.

Each grain boundary element pair was categorised in this way, before being sorted by their misorientation angle into bins of 1° width. The proportion of elements that met the threshold condition $c_i \geq c_o$ was defined as the cavitation ratio. Within the experimental data-set collected by He et al. the average cavitation ratio was 0.27. The value of λ used within the condition seen in Eq. (28) was determined to find the same average cavitation ratio within the simulated microstructure. The Pearson product moment correlation coefficient was calculated to assess the relationship between microstructural and model parameters with the simulated phase field.

Finally, the applicability of the phase field model in predicting which individual grain boundaries were most susceptible to cavitation was assessed with a direct point to point comparison. The location of the two hundred grain boundary elements with the highest phase field damage value within the simulation were plotted alongside the two hundred points most damage points from the experimental specimen overlaid on the same EBSD microstructure. The results are plotted in Fig. 10.

6. Results

The objective of the following analysis detailed below was to assess the applicability of the implemented crystal plasticity phase field approach to predicting damage initiation. Comparisons were drawn between experimental results of He at al., He et al. (2023), on a sample of 316H stainless steel with the reference elastic strain energy damage crystal plasticity phase field model, an elastoplastic strain energy based damage model, a combined creep plasticity deformation model, and a phase field model with a grain misorientation dependent critical energy release rate. Correlations between output model parameters and input microstructural parameters with the phase field damage value at grain boundary elements were determined and compared to those determined experimentally.

In Section 6.1, the reference elastic strain energy damage model was used to find the correlation between the phase field value at grain boundary elements with the Schmid factors of adjacent grains, as well as the loading direction stress, and local densities of statistically stored and geometrically necessary dislocations. Afterwards, the cavitation ratio against boundary misorientation angle is compared with the equivalent experimental analysis alongside a comparison of individual grain boundaries most susceptible to cavitation. Section 6.2 presents analysis of the cavitation ratio and specific grain boundaries including the implementation of a misorientation dependent critical energy release rate, G_c. Finally, Sections 6.3 and 6.4 detail similar analysis for the elastoplastic damage model and creep plasticity deformation model, respectively.

6.1. Reference elastic strain energy damage model

In this section, the reference elastic strain energy damage model, with $\beta = 0$ in (25), is used. A 3D structured mesh consisting of a single layer of elements with a thickness of 5 microns was produced using Euler angles for crystallographic orientation from an EBSD microstructure determined by Martin et al. (2022) for 316H austenitic stainless steel. The reconstructed 3D planar microstructure was generated using MOOSE and is shown in Fig. 4.

The average 2D grain diameter within the EBSD microstructure obtained from the experimental specimen was 44 microns with a standard deviation of 38 microns. The smallest 2D grain diameter found was 3 microns while the largest was 267 microns. The mesh consisted of 170 elements measuring 1020 μm in the X direction and 169 elements measuring 1014 μm in the Y direction. The mesh was one element thick in the z direction with a thickness of 5 μm. In total, the mesh contained 28730 elements, with each element having dimensions of 6 × 6 × 5 μm. The model had tensile boundary conditions applied to simulate uniaxial tensile loading up to 0.15% strain in the positive Y direction, with free boundary conditions applied to positive faces in X and Z. The negative faces in X, Y, and Z were held fixed at zero displacement.

The strain amplitude in the region of interest, which was located close to the notch in the specimen, has been determined using macroscopic finite element simulations in previous works (Demir et al., 2023; He et al., 2023). The reference simulation used the coupled crystal plasticity phase field fracture model considering only the elastic strain energy contributing to damage evolution. This was implemented by setting the plastic work inclusion factor $\beta = 0$. The model and material parameters used are shown in Table 4, including the elastic constants of 316H stainless steel in Voigt notation. The output phase field is also displayed in Fig. 4, showing the accumulated damage under the simulated conditions. The order of magnitude of the phase field was compared to the area fraction of the experimental region of interest that exhibited damage. The SEM micrograph shown in Fig. 4 was analysed pixel by pixel to find the proportion of pixels that were black, which indicated points of damage. The area fraction of the SEM image that was black was 0.000384, whereas the maximum value of the phase field using the reference elastic strain energy damage model was 0.000399.

In Fig. 5(a), the relationship between the average between the Schmid factors (maximum among the slip systems) at pairs of elements across grain boundaries is compared to the phase field damage. In Fig. 5(b), the same is done for the difference between the Schmid factors (maximum among the slip systems). A very weak correlation was found between the phase field damage at grain boundary elements with the average boundary Schmid factor and difference in boundary Schmid factor, in agreement with experimental observations from He et al. (2023). However, it is evident that the range of the damage increases with the average Schmid factor, while it decreases with the difference in Schmid factor, indicating that more plastic activity in the pair of grains is more likely to induce more damage.

A linear regression has been used to provide bounds in each plot for the range within which 95% of the data sits, denoted by the area highlighted in red in Figs. 5, 6, and 7. A simulation including the effect of geometrically necessary dislocations (GNDs) was also run using the reference elastic strain energy damage model to detail the relation to the phase field damage as well as

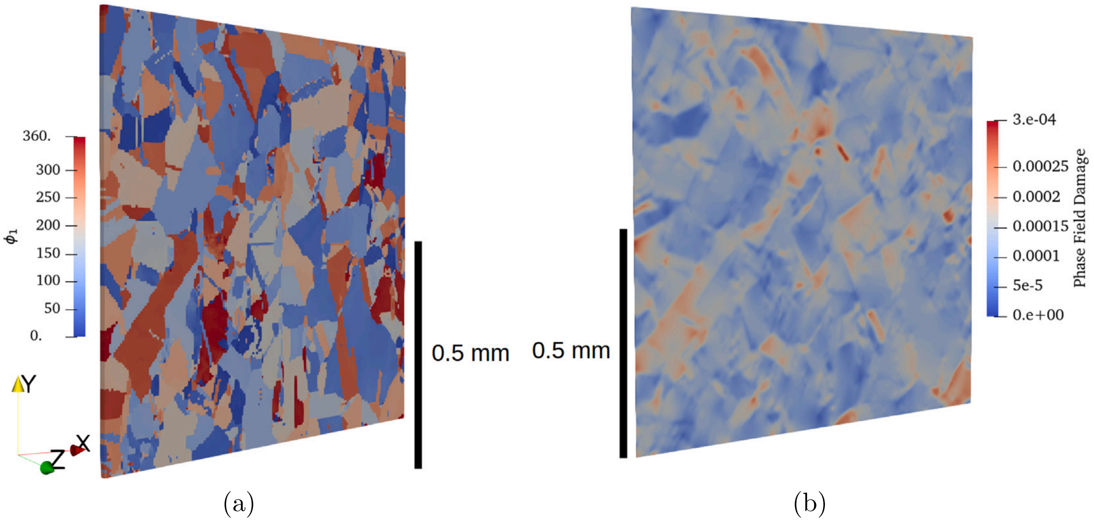

(a)

(b)

Fig. 4. (a) The experimentally determined EBSD microstructure simulated of 316H stainless steel simulated. ϕ_1 denotes the first Euler angle in a ZXZ notation format. (b) The resulting phase field across the microstructure using the reference elastic strain energy damage model.

Table 4
Calibrated material and model parameters.

Number of Elements	28 730
Temperature (T)	823 K
Elastic constant $\mathbb{C}_{11}$ at $T = 550$ °C	204.6 GPa
Elastic constant $\mathbb{C}_{12}$ at $T = 550$ °C	137.7 GPa
Elastic constant $\mathbb{C}_{44}$ at $T = 550$ °C	126.2 GPa
Shear modulus (μ)	86 GPa
Initial SSD density ($\rho^{\alpha}_{\mathrm{SSD}}$)	257.36 $\mu\mathrm{m}^{-2}$
Initial GND Density - Edge ($\rho^{\alpha}_{\mathrm{eGND}}\,(t = 0)$)	0.0 $\mu\mathrm{m}^{-2}$
Initial GND Density - Screw ($\rho^{\alpha}_{\mathrm{sGND}}\,(t = 0)$)	0.0 $\mu\mathrm{m}^{-2}$
Reference Slip Rate ($\dot{\gamma}^{s}_{0}$)	0.001 s^{-1}
Section 6.4 - Reference Creep Slip Rate ($\dot{\gamma}^{c}_{0}$)	$3 \cdot 10^{-8}$ s^{-1}
Slip strain rate sensitivity exponent (m_s)	0.1
Section 6.4 - Creep strain rate sensitivity exponent (m_c)	0.1
Peierls stress (τ^{0}_{c})	0.112 MPa
Burgers vector (b)	0.256 nm
Taylor hardening prefactor (α_0)	0.3
Dislocation accumulation rate (k_m)	1.13
Dislocation Capture Radius (y_c)	1.3 nm
Room temperature (T_0)	293 K
Characteristic Phase Field Model Length-scale (l_0)	3.0 μm
Section 6.1 - Critical Energy Release Rate (G_c) Reference Elastic Strain Energy Damage Model	6200 J m^{-2}
Section 6.3 - Critical Energy Release Rate (G_c) Elastoplastic Damage Model	10500 J m^{-2}
Damage kinetic coefficient (η)	0.001 sm^{-1}

that from statistically stored dislocations (SSDs). Fig. 6 details the relation between SSDs and GNDs at grain boundary elements with the phase field damage value. A strong correlation with the total SSD density and microstructural damage with a coefficient of 0.90 was determined. GNDs were found to have a weaker correlation with a coefficient of 0.46. Fig. 7 shows how grain boundary element stress in the loading direction induces damage. As would be expected, higher stress elements are more susceptible to damage initiation, with a correlation coefficient of 0.47 determined.

6.2. *Grain misorientation dependent critical energy release rate*

Carbide precipitates are known to exacerbate material degradation and intergranular cavitation (Sawada et al., 2019). It has been established that carbide precipitation density varies with the grain boundary misorientation angle, $\Delta\theta$, in various stainless steels experimentally (Hong et al., 2001; Jones et al., 2008; Slater et al., 2017; He et al., 2021), with high angle boundaries of particular interest. By locally varying the value of G_c depending on the boundary misorientation angle, it is possible to model the effect of grain boundary misorientation and the presence of intergranular carbides in the aggregate to more accurately capture both large scale trends in damage initiation as well as predict boundaries and regions more susceptible to early damage formation.

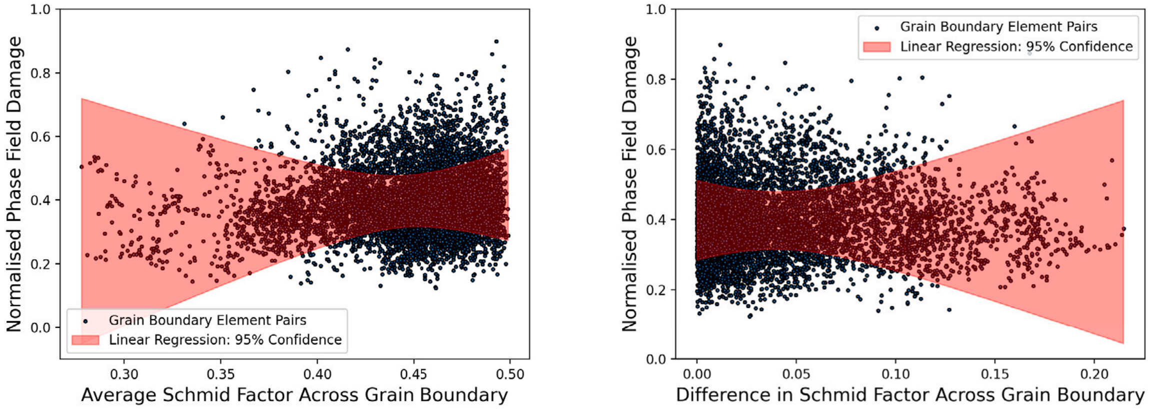

(a)	(b)

Fig. 5. (a) The average between the Schmid factor (maximum among the slip systems) across a grain boundary against grain boundary phase field damage for a number of element pairs. (b) The difference in Schmid factor (maximum among slip systems) across a grain boundary against grain boundary phase field damage for a number of element pairs. (For interpretation of the references to colour in this figure legend, the reader is referred to the web version of this article.)

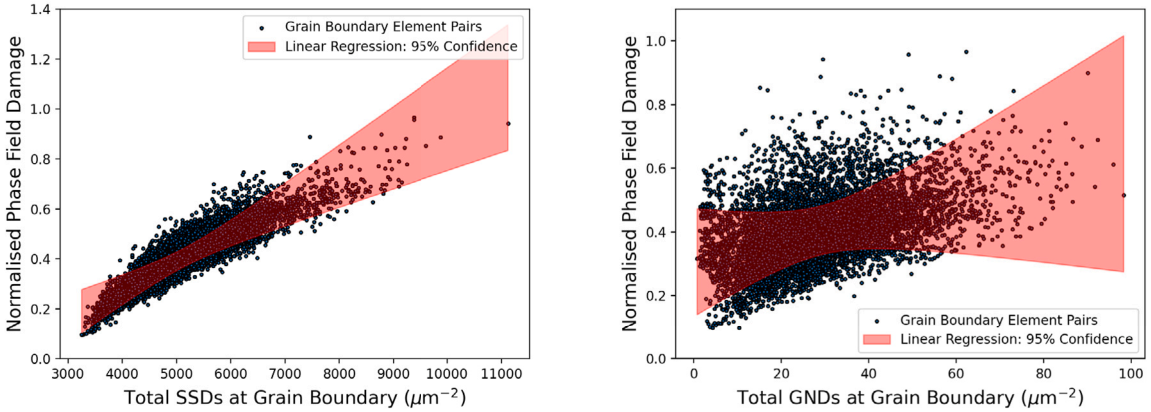

(a)	(b)

Fig. 6. (a) A plot of phase field damage against the density of statistically stored dislocations across a grain boundary. The Pearson product moment correlation coefficient recorded was 0.90. (b) A plot of the normalised phase field damage against the total density of geometrically necessary dislocations (GNDs) across all slip systems at grain boundary elements. The Pearson product moment correlation coefficient calculated was 0.46. (For interpretation of the references to colour in this figure legend, the reader is referred to the web version of this article.)

Typically, grain boundary behaviour is separated into two categories, with mid angle boundaries separated from high and low angle boundaries. This was considered by using a simple model for a local reduction in G_c that varies with grain boundary misorientation angle. A transition point was selected as ten degrees from either end of the profile in Fig. 1, leaving the only free parameter to be varied as the size of the fractional reduction in G_c. By analysing the difference in overall damage trends and adjusting the scale of the reduction in G_c to maximise the Pearson product moment correlation coefficient between the cavitation ratio of the simulation and the experimental data, a quantitative estimate of the reduction in G_c caused by carbide precipitation and grain misorientation can be obtained through computational means. Additionally, linear, and parabolic profiles for G_c were simulated to assess the stability of results to profile shape as well as the minimum value of G_c. The profiles implemented can be seen in Fig. 1. In the following, the maximum and minimum values of $G_c\,(\Delta\theta)$ in Fig. 1(a) will be called G_{c0} and $G_{c\min}$. A range of simulations were run using the reference elastic strain energy damage model, with the minimum value of G_c given by:

$$G_{c\min} = \nu G_{c0}, \tag{29}$$

where ν is a scalar that was varied between 0.5 and 1 describing the fractional value of G_c. The model input parameters were otherwise identical to those used in Section 6.1, which are reported in Table 4.

Fig. 8(a) shows the experimental and simulated grain boundary cavitation ratio as a function of the grain boundary misorientation angle $\Delta\theta$. Different curves represent simulations carried out with different values of $G_{c\min}$ using the trapezoidal profile shown in

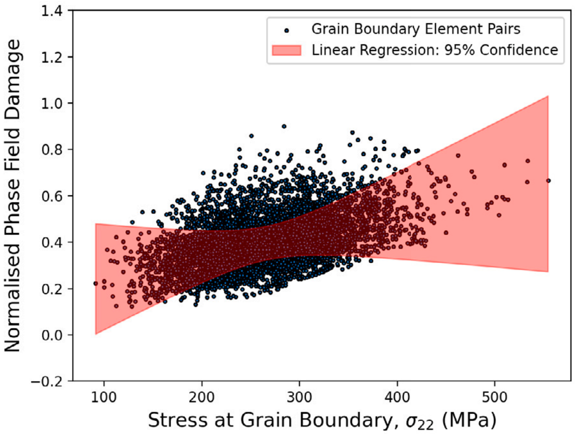

Fig. 7. A plot of the phase field damage at grain boundary elements against the loading direction stress, σ_{22}, in MPa. The Pearson product moment correlation coefficient recorded was 0.47. (For interpretation of the references to colour in this figure legend, the reader is referred to the web version of this article.)

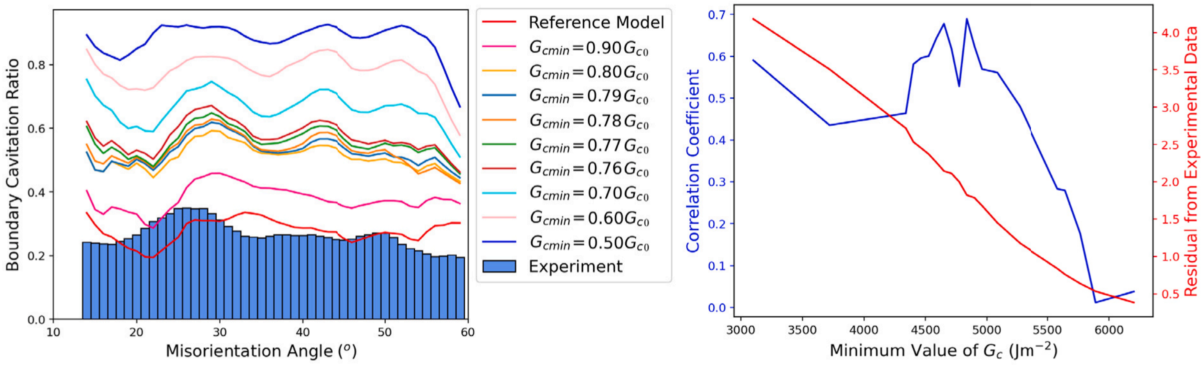

(a)

(b)

Fig. 8. (a) A histogram of the experimentally determined cavitation ratio against boundary misorientation angle in 316H stainless steel compared with the simulated data with varying reductions in the critical energy release rate, G_c, for the trapezoidal profile from Fig. 1. (b) Plots of the correlation coefficient and the residual norm between the experimentally determined cavitation ratio and simulated data against the minimum critical energy release rate implemented. The optimal correlation was 0.69 for $G_c = 0.78G_{c0}$.

Fig. 1. The Pearson product moment correlation coefficient between these two distributions is shown in Fig. 8(b) as a function of G_{cmin}. The threshold value, λ, used to determine cavitation was 0.45. For the analysis here, this value was taken using the uniform G_c model and was applied to subsequent simulations with varying G_c to reflect the increase in cavitation relative to the reference elastic strain energy damage model that occurs because of lowering the critical energy release rate. The same figure reports the residual as a function of G_{cmin}, which is the integral over $\Delta\theta$ of the absolute value of the difference between simulated and experimental data in Fig. 8(a). By varying the minimum value of G_c, the highest correlation of greater than 0.69 was found for $G_{\text{cmin}} = 0.78G_{c0}$. This is a substantial improvement in the correlation compared with the uniform G_c model, which has a correlation coefficient of 0.04 only. It corresponds to intergranular carbides and grain misorientation effects resulting in an approximate 22% local reduction in the critical energy release rate G_c. The optimum value of G_{cmin} found previously was then implemented using the linear and quadratic profiles shown in Fig. 1, with the boundary cavitation ratio shown for both alongside the trapezoidal model, experimental results, and the reference elastic strain energy damage model using an homogeneous G_c in Fig. 9. The highest correlation coefficient obtained was 0.71 using the quadratic profile, with the linear and trapezoidal profiles significantly more accurate than the reference elastic strain energy damage model with correlations of 0.53 and 0.69, respectively.

Using this misorientation dependent value of G_c, a comparison between damage initiation sites within the simulated microstructure was made to the same experimental sample. Fig. 10 shows the EBSD microstructure used, with overlaid scatter plots detailing the two hundred highest damage points within the simulation and experimental structure. The objective of this analysis is to identify which grains and grain boundaries are susceptible to cavitation, not just matching specific elements. Out of eleven grain boundaries exhibiting the most significant cavitation experimentally, one was predicted by the reference elastic strain energy damage model seen in Fig. 10 as red scatter points. The implemented variation in G_c resulted in further two grain boundaries matching experimental cavitation data, seen as green scatter points.

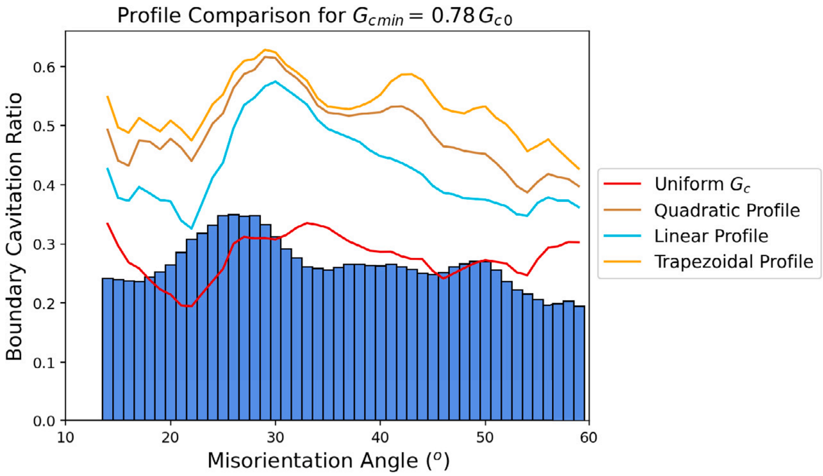

Fig. 9. A histogram of the experimentally determined cavitation ratio against boundary misorientation angle in 316H stainless steel compared with the simulated data using the optimum fit value of $G_{\mathrm{cmin}} = 0.78G_{c0}$ implemented using the linear, quadratic, and trapezoidal profiles from Fig. 1, as well as the reference homogeneous G_c model.

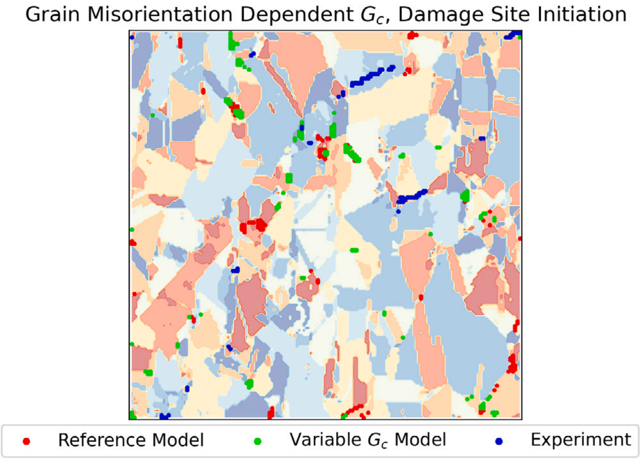

Fig. 10. An EBSD microstructure overlaid with scatter plots of highly damaged regions within experimentally determined cavitation data as well a crystal plasticity simulation with the optimum misorientation dependent critical energy release rate implemented. (For interpretation of the references to colour in this figure legend, the reader is referred to the web version of this article.)

6.3. Comparing the use of an elastoplastic strain energy damage model

The reference elastic strain energy damage model was now used with the plastic work contribution to damage evolution implemented to produce an elastoplastic damage model, which was then applied over the same microstructure with identical input parameters except for $\beta = 1$ in Eq. (25), and the value of G_c, for which the calibrated value of 10500 J m^{-2} was used. The boundary cavitation ratio across grain boundary elements was compared between the two damage models and that found from the experimental microstructure are shown below in Fig. 11.

The cavitation ratio as a function of misorientation angle was determined using a threshold value ν of 0.45 for both the reference elastic strain energy damage model and elastoplastic damage model was determined. A histogram below shows the same metric determined across the same microstructure using the correlative microscopy techniques described in Section 3. The correlations found for the reference elastic strain energy damage model and elastoplastic damage model were 0.04 and 0.03, respectively. At the low strain levels imposed in these simulations, there is limited plastic deformation across the microstructure, meaning that the plastic work contribution term is small relative to that of elastic strain. Since both the reference elastic strain energy damage model and elastoplastic damage model had input values of G_c calibrated to ensure fracture at the same level of strain, the magnitude of the damage in Fig. 11(b) is lower, the pattern of damage initiation simulated in Fig. 11(a) and therefore the damage field obtained is almost identical, resulting in similar correlations with experimental analysis.

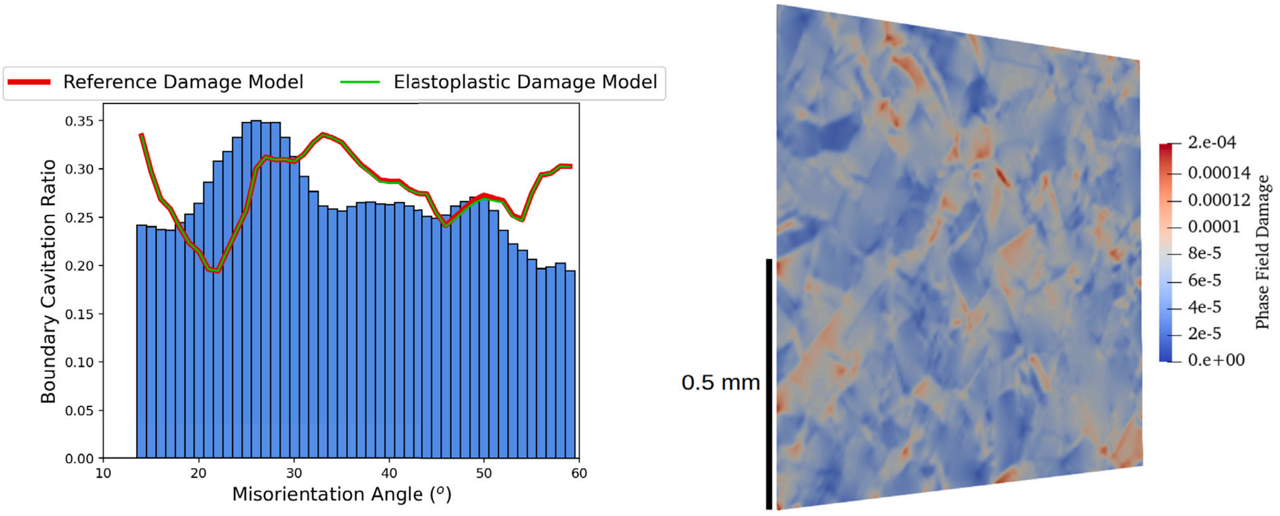

(a) (b)

Fig. 11. (a) Plots of the cavitation ratio against grain boundary misorientation for an experimental sample of 316H stainless steel, compared to the reference elastic strain energy damage model and elastoplastic damage model respectively with correlation coefficients of 0.04 and 0.03, respectively. (b) The damage field produced using the elastoplastic damage model over the microstructure shown in Fig. 4.

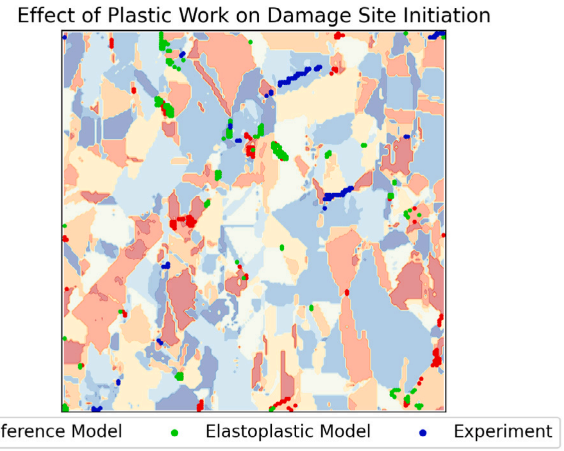

Fig. 12. An EBSD image of the simulated microstructure, with scatter plots detailing grain boundaries meeting the damage threshold from the reference elastic strain energy damage model, the elastoplastic damage model, and experimentally determined cavitation data over the same microstructure. (For interpretation of the references to colour in this figure legend, the reader is referred to the web version of this article.)

Finally, the positions and sites of cavity nucleation determined in an experimental sample were compared to those identified using both the reference elastic strain energy damage model and elastoplastic damage model. An image of the EBSD microstructure is shown in Fig. 12.

Within the EBSD microstructure, there were eleven grain boundaries that exhibited significant cavitation upon considering the two hundred highest points across the structure, seen as black scatter points in Fig. 12. The two hundred highest points within the reference elastic strain energy damage model and elastoplastic damage model are shown as green and red scatter points respectively in Fig. 12. The reference elastic strain energy damage model predicted only one of the eleven grain boundaries of interest, with the introduction of the plastic work contribution improving this to four of the eleven boundaries or grains of interest. It is suspected that large MnS inclusions which are not currently accounted for in the model are responsible for some of the significant cracks observed. See Fig. E.17, where the regions predicted by the elastoplastic damage model that agree with experimental data have been marked.

6.4. Comparing damage initiation due to plasticity and creep deformation

The additional creep deformation term outlined in Eq. (5) in Section 2 was also applied to the same microstructure to examine the difference in damage initiation resulting from the addition of creep deformation alongside plasticity. The boundary conditions and level of total creep strain applied were determined using a component level continuum finite element model with an ABAQUS creep subroutine of the double notched specimen studied by He et al. (2023). This model was used to inform the crystal plasticity model of the average in-plane strain components which were extracted from a 1 mm^2 area from the region between the notch tip and the centre-line of the specimen. Fig. 2 displays the location of the area stated. In the crystal plasticity model the plastic slip term, which is the first term in Eq. (5), is suppressed at a strain level of 0.15%, leaving only the creep deformation term in Eq. (5) active subsequently to reflect long term deformation. The creep deformation term has the same form as the plastic slip term, with different rate constants, see Table 4.

A similar analysis to that of Section 6.3, 6.2, and 6.1 was carried out to determine the cavitation ratio for varying grain boundary misorientation angles. The threshold value in Eq. (28) used to decide if a grain boundary element was exhibiting damage, λ, had a value of 0.33. The resulting plot can be seen in Fig. D.15, which had a correlation of cavitation ratios between the experimental result and creep plasticity deformation model of 0.35, a significant increase on that of the reference elastic strain energy damage model which was 0.04. Finally, the grain boundaries most susceptible to damage within the simulated microstructure were compared to the experimental specimen using the two hundred most damaged points within the simulation and the specimen shown in Fig. D.16. Of the eleven boundaries outlined within the specimen, two were predicted by the creep plasticity deformation model. Not including creep diffusion effects for creep cavitation is justified here due to the stress induced during the experiment of 390 MPa. At this high stress, damage is likely to be dominated by plastic void initiation, making the crystal plasticity phase field approach suitable for this analysis.

7. Discussion

The applicability of a continuous damage variable such as a phase field to modelling the distribution of discrete voids is a matter of debate, with little precedent established within the literature, although this has been attempted for other modelling techniques (Bouchard et al., 2004). The interpretation of the phase field as it pertains to void initiation was critical for the analysis presented here. As is commonly done with phase field formulations, the stiffness tensor is locally modified depending on the phase field value by applying a degradation function, usually of a quadratic form as in equation:

$$\mathbb{C} \rightarrow (1 - c^2)\mathbb{C} \tag{30}$$

This can be seen as analogous to a local loss in material or crystalline structure at this point, which causes the reduction in elastic constants and local stress, therefore allowing for correlation with void initiation within the mesoscale structure. There is very little work within the literature applying phase field models to modelling early damage formation as compared to experimental data. As such, the point at which void initiation is said to have taken place was based on a novel cavitation damage threshold chosen by the authors within this work, but other approaches could also be used here. Furthermore, the evolution of the phase field is subject to interpretation. The characteristic length-scale in Eq. (25), l_0, dictates the diffuseness of the phase field. A low l_0 results in point like damage formation of high intensity that could be seen as more accurately representing void initiation, without allowing the damage field to evolve and spread that is critical for void nucleation and growth when modelling ductile failure. Similarly, issues are associated with a large l_0. Here, damage is too diffuse, facilitating void coalescence type behaviour at the cost of preventing discrete crack path definition and growth. The effect of varying the characteristic length-scale on damage initiation within the model framework presented here is shown in Appendix C. While increasing the length-scale did increase the correlation in the cavitation ratio compared to the reference model from 0.04 to 0.24, the effect is significantly smaller than other effects such as grain misorientation and varying the critical energy release rate. While increasing the value of l_0 affects the phase field at the small grain size length scale, this effect is mitigated by the distribution of grain sizes within this microstructure as well as the large number of points such that the results and conclusions are not significantly affected. Furthermore, the work of others including Miehe et al. (2010b) establishes the limitations for reducing l_0 further than has been used within the work presented here. This is because of physical considerations between the value of l_0 and the element size. Since l_0 acts as the regularisation factor of a crack length, reducing the value of this term further below the mesh size is not required.

The goal of this work was to establish a framework in which by accounting for certain degradation mechanisms within a material, phase field models would be suitable to modelling early damage initiation. The growth and ductile failure of creep cavities formed as a result of intergranular carbides at grain boundaries, as well as the formation and failure due to plastic strain induced voids were accounted for using a grain boundary misorientation dependent value of the critical energy release rate. The application to an experimental 316H stainless steel sample was used to demonstrate the potential of this approach. Electron backscatter diffraction measurements were used to identify a grain microstructure in the experimental specimen. The microstructure was recreated in crystal plasticity and trends in damage initiation were directly compared between simulation and experiment.

An initial value of the critical energy release rate was determined by plotting the relationship between the initial value of G_c with the macroscopic strain for failure, which can be seen Fig. 3. This relationship was then interpolated to find the value of G_c that reproduces the strain for failure of 316H stainless steel. The work presented here examines the extent to which the macroscopic value of G_c can be used to reproduce microstructural behaviour, and the extent to which it can be applied is an avenue for further work in this area. The potential drawback to this approach is whether or not the macroscopic failure occurs via a sufficiently different mechanism that an alternative value for the microstructural critical energy release rate is required.

However, by implementing a misorientation dependent critical energy release rate, G_c, a much stronger correlation was found with the experimentally determined cavitation ratio of 0.67, compared with little to no correlation observed with the reference elastic strain energy damage model and elastoplastic damage model from Sections 6.1 and 6.3, both of which used a constant value of G_c. This suggests that when local variation in G_c is introduced, CPFE approaches have significant potential to capturing plastic void initiation behaviour associated with grain boundaries observed experimentally. The sensitivity of the profile shape used for the critical energy release rate was examined. With the relation between the simulated and experimental cavitation ratio varying by up to 26% when comparing the trapezoidal, linear, and quadratic profiles exhibited in Fig. 9. This further outlines the importance of adding accurate experimental data characterising the precipitation rate of carbides along grain boundaries of different misorientation angles, which would allow for a more precise determination of the reduction in the critical energy release rate attributable to a specific carbide density. It should be noted that due to the large microstructural region with more than three thousand grain boundary elements, as well as the interlinking effects within the crystal plasticity model implemented, the likelihood of obtaining high Pearson product moment correlation coefficients between two model parameters is reduced. This is in a similar manner to that of Zhang et al. who applied machine learning techniques to determine grain boundary susceptibility to damage (Zhang et al., 2022).

The correlation of SSD and GND density with simulated damage indicates that grain boundary pile up and plasticity are key influencing factors on damage formation within the model framework presented here. As a means of identifying factors predictive of damage within the phase field model, it should be noted that Figs. 6 and 7 predict a minimum value of the phase field at a particular grain boundary element based on the value of SSD density, GND density, or loading direction stress. The effect microstructural factors such as the average value and difference in Schmid factors of adjacent grains on damage were also considered, with little correlation found. This matches the findings over the same microstructure in an experimental sample by He et al. (2023), who observed no significant correlation between damage formation and Schmid factor values of adjacent grains.

Limitations in application of this framework to experimental results relate mostly to the availability of experimental data allowing for further inclusion of microstructural features and effects that contribute to damage formation. For example, elongated manganese sulphide (MnS) inclusions that can form across grains and grain boundaries in 316H stainless steel can cause stress concentrations leading to void nucleation in both grains and grain boundaries through local variations in elastic material properties. Such inclusions have not been accounted for in the crystal plasticity model outlined in this work. Including the effect of inclusions such as MnS could allow for more accurate prediction of grain boundaries particularly susceptible to damage initiation.

These features could be characterised through a scanning electron microscopy (SEM) and energy dispersive X-ray spectroscopy (EDX) study before implementation into the initial starting microstructure for finite element analysis, but such data was not available for the work shown here. It is suspected that the limited accuracy of predicting specific grain boundaries that exhibited void initiation are possibly due to inclusions, but further testing would be required to examine exactly which voids within the real specimen had inclusions present using EDX analysis.

The subsurface microstructure and boundary conditions on a specimen have been discussed within the literature as an influencing factor in the surface stress field, with differing stress states known to have an impact upon damage initiation (Lian et al., 2014). The effect of varying subsurface microstructure is explored in Appendix C. The correlation in cavitation ratio with boundary misorientation increased from 0.04 to up to 0.78 depending on the substructure. This indicates that the effect of subsurface microstructure on damage initiation is as significant within the presented model framework as grain misorientation. What cannot be precisely recreated within the model framework at present is the effect of boundary conditions resulting from a large scale microstructure. Further experimental characterisation using successive EBSD and focused ion beam scans to produce a full 3D reconstruction of a target area within the specimen.

One difficulty with the comparison of simulations with experimental data shown here was the loading history of the sample, resulting in significant complexity in active degradation mechanisms causing damage. Planned future work will include applying this model framework and similar experimental analysis on a specimen subjected only to tensile load, before then recreating a section of the microstructure for simulations using the same CPFE model. The goal of which is to examine a sample purely in tension, in which plasticity alone causes microstructural degradation. This study may also allow for the calibration of the relative contribution to damage formation of plastic work compared to elastic strain energy. At present, the plastic work term included is given equal weighting to the elastic strain energy term in Eq. (25) with β=1, but a study to more accurately calibrate the value of β would be of interest. Furthermore, the relative contribution of creep deformation also requires further investigation to accurately calibrate the relative size of its contribution to damage initiation.

Further work can also include improvements to the existing model framework. Void nucleation is not typically seen until high levels of plastic strain are incurred in a specimen. The models here were run to low levels of strain of 0.15%. Typically, this mismatch in strain levels leading to damage initiation is addressed using a strain damage threshold to limit damage initiation until higher strains are reached. While a strain-based threshold was not included for the work shown here, it is something to be addressed for future applications to other materials and loading modes. Following on from this, variations in damage initiation resulting from specimen geometry and stress triaxiality also present avenues for further work. Moreover, there is evidence within the literature that the influence of carbides on damage nucleation can be exacerbated by intergranular residual stress fields (Pommier et al., 2016), as well as affecting the formation of creep damage (Price et al., 2009). The determination and inclusion of grain to grain residual stresses and their effect on damage initiation within the existing model presents an additional avenue for further work.

8. Conclusions

A novel approach to apply crystal plasticity phase field modelling techniques to damage initiation has been implemented. To assess the applicability of this framework to modelling early damage formation, this approach has been applied and compared to experimental cavitation results across the same microstructure obtained with correlative electron microscopy techniques. Analysis correlating the damage field across a microstructure of 316H stainless steel has been done to identify correlations between the phase field damage value and microstructural and model characteristics including the Schmid factors, dislocation densities and loading direction stress at grain boundaries. A very strong correlation between the SSD density and phase field damage of 0.90 was found along these grain boundary elements, with GND density correlated to a lesser extent with 0.46. Correlations obtained for the Schmid factors for adjacent grains with the phase field damage returned no correlation, a result matching experimental observation.

A novel threshold was used to infer cavitation across a simulated microstructure damage field to calculate the proportion of grain boundaries that exhibited cavitation as a function of the grain boundary misorientation angle, known as the cavitation ratio. To model the effect of grain misorientation on damage, alongside intergranular carbides which are too small to be explicitly modelled using mesoscale crystal plasticity simulations, an aggregated approach was used. This was in the form of a misorientation dependent value of the critical energy release rate was able to greatly improve the correlation of this metric with experimental data from 0.04 to 0.71, suggesting that the effect of misorientations and carbide precipitation has a strong influence in early damage and cavity nucleation.

The size of the local variation in the energy release rate G_c was varied to find the value of G_c that returned the highest correlation against experimental data for the cavitation ratio as a function of the grain boundary misorientation angle. The local reduction in G_c along grain boundaries due to misorientation effects and carbide precipitation was up to 22%. Due to a lack of literature data detailing precipitation rates along grain boundaries of varying misorientation, the variable energy release rate was implemented using an assumed profile. The effect of changing the profile shape was investigated, and the correlation of the cavitation ratio to the misorientation angle was found to vary by up to 26% with different profile shapes. This underlines the need for further experimental investigation characterising intergranular precipitation behaviour of 316H stainless steel along grain boundaries of different misorientation angles.

Model variations such as those including the contribution to damage resulting from plastic deformation and a creep deformation term were also considered. The inclusion of creep deformation alongside plasticity improved the correlation of the cavitation ratio from 0.04 to 0.35, whereas the plastic work inclusion had no significant effect.

The grain boundaries most susceptible to cavitation within a real specimen of 316H were determined, and the ability of the phase field model variations to predict the same boundaries as high in damage was examined. From this, it can be suggested that elastic strain energy does not accurately map this behaviour, which is better described by plastic work contributing to damage as well as local reductions in G_c due to grain misorientation and carbide precipitation, although the improvement in the accuracy of the presented approach requires further investigation to incorporate additional microstructural defects and degradation mechanisms to the model.

CRediT authorship contribution statement

Michael Salvini: Conceptualization, Formal analysis, Investigation, Methodology, Writing – original draft, Writing – review & editing, Visualization. **Nicolò Grilli:** Conceptualization, Methodology, Software, Supervision, Writing – original draft, Writing – review & editing. **Eralp Demir:** Methodology, Software, Writing – review & editing. **Siqi He:** Investigation. **Tomas Martin:** Conceptualization, Writing – review & editing. **Peter Flewitt:** Writing – review & editing. **Mahmoud Mostafavi:** Conceptualization, Writing – review & editing. **Christopher Truman:** Supervision, Writing – review & editing. **David Knowles:** Conceptualization, Writing – review & editing.

Declaration of competing interest

The authors declare that they have no known competing financial interests or personal relationships that could have appeared to influence the work reported in this paper.

Data availability

Data will be made available on request.

Acknowledgements

M.S. acknowledges the support by the EPSRC Center for Doctoral Training in Nuclear Energy Futures. The authors thank Prof. Emilio Martínez Pañeda and Dr. Sergio Lucarini for useful discussions about the phase field fracture model. M.M., D.K., E.D., N.G. acknowledge the support by the SINDRI partnership, EPSRC grant EP/V038079/1.

Appendix A. Jacobian calculation with damage

The Jacobian of the Newton–Raphson algorithm that determines the stress and plastic deformation at each time step is calculated by slightly modifying the method described in Balasubramanian (1995). In this section, sum over repeated indices is assumed. The Cauchy stress $\boldsymbol{\sigma}$ is related to the 2nd Piola–Kirchhoff in (24) by:

$$\boldsymbol{\sigma} = \frac{1}{\det\left(\boldsymbol{F}_e\right)} \boldsymbol{F}_e \, \boldsymbol{S} \, \boldsymbol{F}_e^T \ . \tag{A.1}$$

The variable that is updated at each iteration step is the Cauchy stress and the material tangent, $\mathbf{W}$, which is a fourth rank tensor, is defined as the partial derivative of the Cauchy stress with respect to a relative strain increment or stretch increment tensor, $\boldsymbol{\Delta U}$, as in Eq. (A.2):

$$\mathbf{W} = \frac{\partial \boldsymbol{\sigma}}{\partial \boldsymbol{\Delta U}} \quad \Rightarrow \quad \partial \sigma_{ij} = W_{ijkl} \, \partial \Delta U_{kl} \ \text{ in index notation.} \tag{A.2}$$

The $\boldsymbol{\Delta U}$ is defined as the stretch increment in one time step in the co-rotational reference frame (Grilli et al., 2019, 2020). It can be expressed mathematically by the relationship:

$$\Delta F_{ij} = \Delta R_{ik} \, \Delta U_{kj} \ , \tag{A.3}$$

where ΔF_{ij} are the components of the increment of the deformation gradient and ΔR_{ij} is the relative rotation increment, determined using the polar decomposition.

The variation of the Cauchy tensor is given by (A.4):

$$\partial \boldsymbol{\sigma} = \frac{1}{\det \mathbf{F}_e} \left[\partial \mathbf{F}_e \, \mathbf{S} \, \mathbf{F}_e^T + \mathbf{F}_e \, \partial \mathbf{S} \, \mathbf{F}_e^T + \mathbf{F}_e \, \mathbf{S} \, \partial \mathbf{F}_e^T - \left(\mathbf{F}_e \, \mathbf{S} \, \mathbf{F}_e^T \right) \partial \mathbf{F}_e \ : \ \mathbf{F}_e^{-1} \right] \ . \tag{A.4}$$

In the following the indices characterising the components of the matrix $\mathbf{F}_e$ will be shown as subscript to avoid confusion with the pedix “e”. It is useful to define two additional fourth rank tensors P_{ijkl} and Q_{ijkl} as in (A.5) and (A.6):

$$P_{ijkl} = \frac{\partial F^e_{ij}}{\partial \Delta U_{kl}} \ , \tag{A.5}$$

$$Q_{ijkl} = \frac{\partial S_{ij}}{\partial \Delta U_{kl}} \ . \tag{A.6}$$

Substituting (A.5) and (A.6) into (A.4), the Jacobian in index notation becomes as in (A.7):

$$\begin{aligned} W_{ijkl} = \frac{1}{\det \mathbf{F}_e} \Big[& P_{imkl} \, S_{mn} \, F^e_{jn} + F^e_{im} \, Q_{mnkl} \, F^e_{jn} + \\ & F^e_{im} \, S_{mn} \, P_{jnkl} - F^e_{im} \, S_{mn} \, F^e_{jn} \, P_{pqkl} F^{-1\ e}_{qp} \Big] \ . \end{aligned} \tag{A.7}$$

i. Calculation of $P_{ijkl} = \partial F^e_{ij} / \partial \Delta U_{kl}$

To calculate P_{ijkl}, the elastic part of the deformation gradient is expressed in terms of the relative stretch as in (A.8), in which $F^e_{ij}(t)$, S^β_{ij} and $\Delta\gamma^\beta$ represent the elastic deformation gradient at the former time step, the Schmid tensor and the slip increment of the slip system β respectively:

$$F^e_{ij} = \Delta R_{ik} \, \Delta U_{kl} \, F^e_{lm}(t) \left[\delta_{mj} - \sum_{\beta=1}^{N_s} \Delta\gamma^\beta \, S^\beta_{mj} \right] \ . \tag{A.8}$$

Differentiation of (A.3) with respect to the relative stretch gives Eq. (A.9):

$$P_{ijkl} = \Delta R_{ik} \, F^e_{lj}(t) - \Delta R_{ik} \, F^e_{lp}(t) \sum_{\beta=1}^{N_s} \Delta\gamma^\beta \, S^\beta_{pj} - \Delta R_{im} \, \Delta U_{mn} \, F^e_{np}(t) \sum_{\beta=1}^{N_s} T^\beta_{kl} \, S^\beta_{pj} \ , \tag{A.9}$$

in which T^β_{kl} is the differential expressed as in (A.10):

$$T^\beta_{kl} = \frac{\partial \Delta\gamma^\beta}{\partial \Delta U_{kl}} \ . \tag{A.10}$$

ii. Calculation of $Q_{ijkl} = \partial S_{ij} / \partial \Delta U_{kl}$

First an additional second order tensor A_{ij} is defined:

$$A_{ij} = F^e_{mi}(t) \, \Delta U_{nm} \, \Delta U_{np} F^e_{pj}(t) \ , \tag{A.11}$$

together with the so-called coefficient matrix for corrector term C^β_{ij}, which is an extension for the phase field damage model of the corrector term presented in Kalidindi et al. (1992):

$$C^\beta_{ij} = \begin{cases} \frac{1}{2} \, (1-c)^2 \, C_{ijkl} \left(A_{km} \, S^\beta_{ml} + S^\beta_{nk} A_{nl} \right) \ , & \text{if } J_e \geq 1 \ , \\ \frac{1}{2} \, C_{ijkl} \left(A_{km} \, S^\beta_{ml} + S^\beta_{nk} A_{nl} \right) \ , & \text{if } J_e < 1 \ , \end{cases} \tag{A.12}$$

where C_{ijkl} denotes the individual components of the fourth-order stiffness tensor $\mathbb{C}$. To find Q_{ijkl}, first the expression for the 2nd Piola–Kirchhoff stress is defined in (A.13), in which S^{tr}_{ij} and C^{α}_{ij} represent the trial stress and coefficient matrix for corrector term:

$$S_{ij} = S^{\mathrm{tr}}_{ij} - \sum_{\beta=1}^{N_s} \Delta\gamma\, C^{\beta}_{ij} \,. \tag{A.13}$$

After differentiating with respect to ΔU_{kl}, (A.14) is obtained in which Q_{ijkl} is expressed as:

$$Q_{ijkl} = D_{ijkl} - \sum_{\beta} C^{\beta}_{ij}\, T^{\beta}_{mn} \sum_{\beta=1}^{N_s} \Delta\gamma^{\beta} J^{\beta}_{mnkl} \,. \tag{A.14}$$

where:

$$D_{ijkl} = \frac{\partial S^{\mathrm{tr}}_{ij}}{\partial \Delta U_{kl}} \,, \tag{A.15}$$

and:

$$J^{\beta}_{ijkl} = \frac{\partial C^{\beta}_{ij}}{\partial \Delta U_{kl}} \,, \tag{A.16}$$

which represent differentials of the trial stress and corrector terms respectively.

iii. Calculation of $D_{ijkl} = \partial S^{\mathrm{tr}}_{ij} / \partial \Delta U_{kl}$

Trial stress is computed using the components, C_{ijkl}, of the fourth-order stiffness tensor, $\mathbb{C}$, and the damage phase field:

$$S^{\mathrm{tr}}_{ij} = \begin{cases} \frac{1}{2}(1-c)^2\, C_{ijkl}\left[A_{kl} - \delta_{kl}\right] \,, & \text{if } J_e \geq 1 \,, \\ \frac{1}{2} C_{ijkl}\left[A_{kl} - \delta_{kl}\right] \,, & \text{if } J_e < 1 \,, \end{cases} \tag{A.17}$$

where δ_{ij} is the identity matrix. Differentiating (A.17) with respect to the stretch increment reveals (A.18):

$$D_{ijkl} = \begin{cases} \frac{1}{2}(1-c)^2\, C_{ijmn}\, L_{mnkl} \,, & \text{if } J_e \geq 1 \,, \\ \frac{1}{2} C_{ijmn}\, L_{mnkl} \,, & \text{if } J_e < 1 \,, \end{cases} \tag{A.18}$$

in which L_{ijkl} is the differential shown in (A.19):

$$L_{ijkl} = \frac{\partial A_{ij}}{\partial \Delta U_{kl}} \,. \tag{A.19}$$

iv. Calculation of $L_{ijkl} = \partial A_{ij} / \partial \Delta U_{kl}$

A_{ij} is the same expression in Kalidindi et al. (1992) but written in terms of the relative stretch tensor and former elastic part of the deformation gradient as in Eq. (A.11). Its derivative gives:

$$L_{ijkl} = F^{e}_{ki}(t)\, \Delta U_{lm}\, F^{e}_{mj}(t) + F^{e}_{mi}(t)\, \Delta U_{mk}\, F^{e}_{lj}(t) \,. \tag{A.20}$$

v. Calculation of $J^{\beta}_{ijkl} = \partial C^{\beta}_{ij} / \partial \Delta U_{kl}$

Differentiating (A.12) gives:

$$J^{\beta}_{ijkl} = \begin{cases} \frac{1}{2}(1-c)^2\, C_{ijmn}\left(L_{mpkl}\, S^{\beta}_{pn} + S^{\beta}_{pm} L_{pnkl}\right) \,, & \text{if } J_e \geq 1 \,, \\ \frac{1}{2}\, C_{ijmn}\left(L_{mpkl}\, S^{\beta}_{pn} + S^{\beta}_{pm} L_{pnkl}\right) . \,, & \text{if } J_e < 1 \,. \end{cases} \tag{A.21}$$

v. Calculation of $T^{\beta}_{ij} = \partial \Delta\gamma^{\beta} / \partial \Delta U_{ij}$

Using chain rule, (A.22) is obtained:

$$T^{\beta}_{ij} = \frac{\partial \Delta\gamma^{\beta}}{\partial S_{kl}} \frac{\partial S_{kl}}{\partial \Delta U_{ij}} \,. \tag{A.22}$$

giving Eq. (A.23)

$$T^{\beta}_{ij} = B^{\beta}_{kl}\, Q_{klij} \,, \tag{A.23}$$

in which B^{β}_{kl} is given by (A.24):

$$B^{\beta}_{ij} = \frac{\partial \Delta\gamma^{\beta}}{\partial S_{ij}} = \frac{\partial \Delta\gamma^{\beta}}{\partial \tau^{\beta}} \frac{\partial \tau^{\beta}}{\partial S_{ij}} = \frac{1}{2} \frac{\partial \Delta\gamma^{\beta}}{\partial \tau^{\beta}} \left(S^{\beta}_{ij} + S^{\beta}_{ji}\right) \,, \tag{A.24}$$

and:

$$Q_{klij} = \frac{\partial S_{kl}}{\partial \Delta U_{ij}} \,. \tag{A.25}$$

Note that $\partial \Delta\gamma^{\beta} / \partial \tau^{\beta}$ can be obtained from the slip constitutive law.

vi. Calculation of $Q_{ijkl} = \partial S_{ij}/\partial \Delta U_{kl}$

Substituting (A.23) for the expression of T^{β}_{kl} into (A.14) reveals (A.26):

$$Q_{ijkl} = D_{ijkl} - \sum_{\beta=1}^{N_s} C^{\beta}_{ij} B^{\beta}_{mn} Q_{mnpq} \sum_{\beta=1}^{N_s} \Delta\gamma^{\beta} \boldsymbol{J}^{\beta}_{pqkl} \,. \tag{A.26}$$

Re-arranging the terms to solve for Q_{ijkl} gives (A.27):

$$\left[\delta_{im}\delta_{jn} + \sum_{\beta=1}^{N_s} C^{\beta}_{ij} B^{\beta}_{mn}\right] Q_{mnkl} = \left(D_{ijkl} - \sum_{\beta=1}^{N_s} \Delta\gamma^{\beta} \boldsymbol{J}^{\beta}_{ijkl}\right) , \tag{A.27}$$

in which an inversion of the first term on the left hand side can be carried out by first transforming the fourth rank tensor into a matrix by using Voigt notation convention, then applying an inversion operation. The tensors P_{ijkl} and Q_{ijkl} are then used to compute the Jacobian in Eq. (A.7). Note that the effect of the damage phase field appears in (A.12), (A.17), (A.18), (A.21).

Appendix B. FCC structure grain boundary misorientation symmetry

This appendix reports the symmetry matrices $\boldsymbol{G}_i$ that are used to calculate the misorientation angle $\Delta\theta$ in Section 2.4 (Pang et al., 2022). They correspond to the 432 FCC crystal symmetries, i.e. they represent the complete set of rigid body motions that transform the crystal into itself. These 24 matrices represent the following operations: identity; inversion with respect to the centre of the cube; 180 degrees rotation around the 3 dyad axes perpendicular to the faces of the cube; 180 degrees rotation around the 3 dyad axes passing through the mid points of the edges of the cube; 120 degrees rotation around the 4 triad axes passing through pairs of vertices of the cube; 90 degrees rotation around the x, y, z axes; reflections with respect to the x, y, z axes; 6 diagonal planes of symmetry that pass through two opposite edges of the cube. They are given by:

$$\boldsymbol{G}_1 = \begin{pmatrix} 1 & 0 & 0 \\ 0 & 1 & 0 \\ 0 & 0 & 1 \end{pmatrix} \quad \boldsymbol{G}_2 = \begin{pmatrix} -1 & 0 & 0 \\ 0 & -1 & 0 \\ 0 & 0 & -1 \end{pmatrix} \quad \boldsymbol{G}_3 = \begin{pmatrix} 1 & 0 & 0 \\ 0 & -1 & 0 \\ 0 & 0 & -1 \end{pmatrix} \tag{B.1}$$

$$\boldsymbol{G}_4 = \begin{pmatrix} -1 & 0 & 0 \\ 0 & 1 & 0 \\ 0 & 0 & -1 \end{pmatrix} \quad \boldsymbol{G}_5 = \begin{pmatrix} -1 & 0 & 0 \\ 0 & -1 & 0 \\ 0 & 0 & 1 \end{pmatrix} \quad \boldsymbol{G}_6 = \begin{pmatrix} 0 & 1 & 0 \\ 1 & 0 & 0 \\ 0 & 0 & -1 \end{pmatrix}$$

$$\boldsymbol{G}_7 = \begin{pmatrix} 0 & 0 & 1 \\ 0 & -1 & 0 \\ 1 & 0 & 0 \end{pmatrix} \quad \boldsymbol{G}_8 = \begin{pmatrix} -1 & 0 & 0 \\ 0 & 0 & 1 \\ 0 & 1 & 0 \end{pmatrix} \quad \boldsymbol{G}_9 = \begin{pmatrix} 0 & 0 & 1 \\ 1 & 0 & 0 \\ 0 & 1 & 0 \end{pmatrix}$$

$$\boldsymbol{G}_{10} = \begin{pmatrix} 0 & 0 & -1 \\ -1 & 0 & 0 \\ 0 & 1 & 0 \end{pmatrix} \quad \boldsymbol{G}_{11} = \begin{pmatrix} 0 & 0 & -1 \\ 1 & 0 & 0 \\ 0 & -1 & 0 \end{pmatrix} \quad \boldsymbol{G}_{12} = \begin{pmatrix} 0 & 0 & 1 \\ -1 & 0 & 0 \\ 0 & -1 & 0 \end{pmatrix}$$

$$\boldsymbol{G}_{13} = \begin{pmatrix} 1 & 0 & 0 \\ 0 & 0 & -1 \\ 0 & 1 & 0 \end{pmatrix} \quad \boldsymbol{G}_{14} = \begin{pmatrix} 0 & 0 & 1 \\ 0 & 1 & 0 \\ -1 & 0 & 0 \end{pmatrix} \quad \boldsymbol{G}_{15} = \begin{pmatrix} 0 & -1 & 0 \\ 1 & 0 & 0 \\ 0 & 0 & 1 \end{pmatrix}$$

$$\boldsymbol{G}_{16} = \begin{pmatrix} -1 & 0 & 0 \\ 0 & 1 & 0 \\ 0 & 0 & 1 \end{pmatrix} \quad \boldsymbol{G}_{17} = \begin{pmatrix} 1 & 0 & 0 \\ 0 & -1 & 0 \\ 0 & 0 & 1 \end{pmatrix} \quad \boldsymbol{G}_{18} = \begin{pmatrix} 1 & 0 & 0 \\ 0 & 1 & 0 \\ 0 & 0 & -1 \end{pmatrix}$$

$$\boldsymbol{G}_{19} = \begin{pmatrix} 0 & 0 & -1 \\ 0 & 1 & 0 \\ -1 & 0 & 0 \end{pmatrix} \quad \boldsymbol{G}_{20} = \begin{pmatrix} 0 & 0 & 1 \\ 0 & 1 & 0 \\ 1 & 0 & 0 \end{pmatrix} \quad \boldsymbol{G}_{21} = \begin{pmatrix} 1 & 0 & 0 \\ 0 & 0 & -1 \\ 0 & -1 & 0 \end{pmatrix}$$

$$\boldsymbol{G}_{22} = \begin{pmatrix} 1 & 0 & 0 \\ 0 & 0 & 1 \\ 0 & 1 & 0 \end{pmatrix} \quad \boldsymbol{G}_{23} = \begin{pmatrix} 0 & -1 & 0 \\ -1 & 0 & 0 \\ 0 & 0 & 1 \end{pmatrix} \quad \boldsymbol{G}_{24} = \begin{pmatrix} 0 & 1 & 0 \\ 1 & 0 & 0 \\ 0 & 0 & 1 \end{pmatrix}$$

Appendix C. Effect of the characteristic regularisation length-scale and subsurface microstructure

The characteristic length-scale, l_0, of the phase field model in Eq. (25) determines the diffuseness of damage across the microstructure. To examine the effect that this length-scale has on results outlined within this paper, a parametric study was run to compare the effect of varying l_0 on the cavitation ratio. The results of which are shown in Fig. C.14(b).

Additionally, it is thought that the subsurface microstructure is a complicating factor in how damage initiates across a microstructure. This is not included in the reference simulation, where only the two dimensional EBSD data is used, which allows only for surface data to be reproduced within crystal plasticity. A series of 3D microstructures were generated by taking the original EBSD microstructure and layering a second layer of elements underneath as shown in Fig. C.13. The effect of the subsurface was varied by changing the texture of the bottom layer. One has the same microstructure added as an identical layer underneath, another

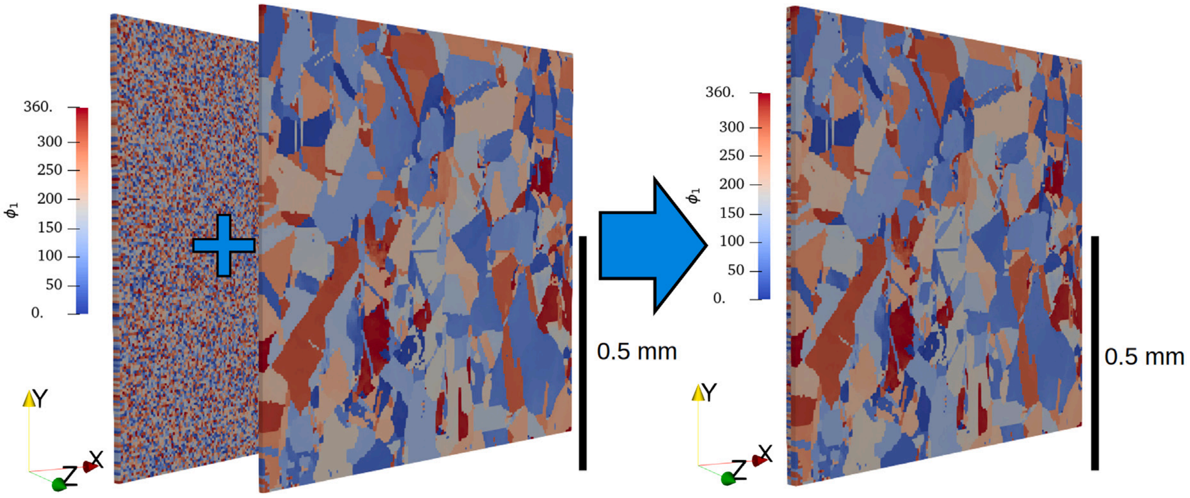

Fig. C.13. An example of how a different substructure was implemented underneath the EBSD microstructure. The plus sign denotes how the subsurface is added to create a two element thick mesh. The random orientation substructure is shown here for reference.

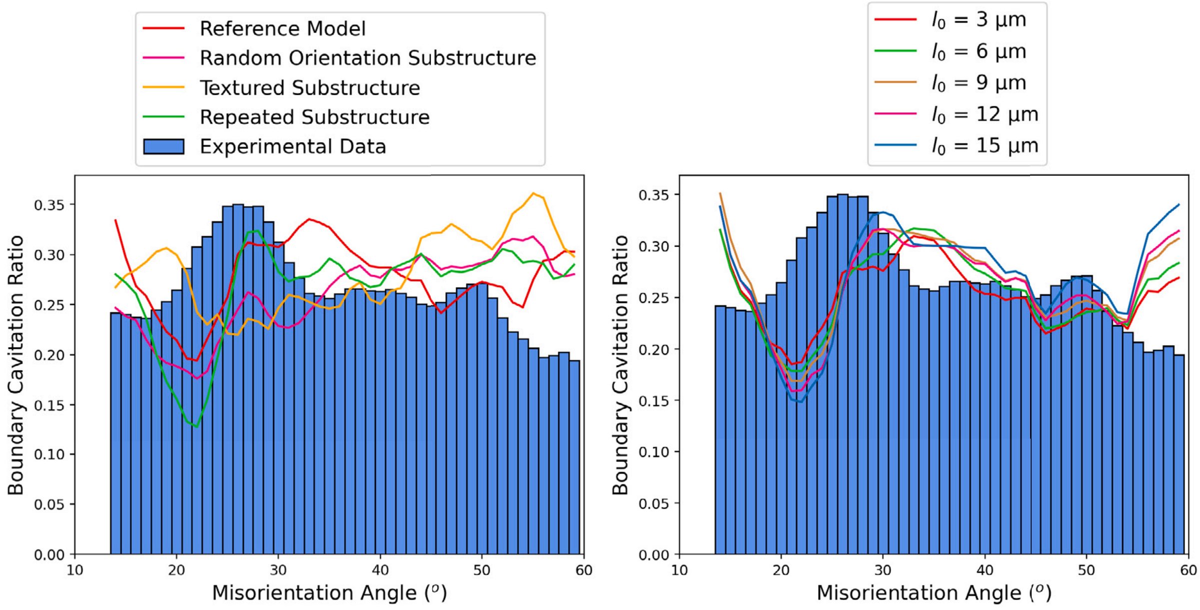

(a) (b)

Fig. C.14. (a) Comparing the experimentally determined cavitation ratio with boundary misorientation angle for a 316H specimen with both the single layer reference model and models with varying subsurface microstructures. (b) Comparing how the cavitation ratio varies with boundary misorientation angle against for varying values of the phase field model characteristic length-scale l_0.

has a similarly textured microstructure, and the last was a layer consisting of randomly oriented elements with no grain morphology features. The modified microstructures were simulated under the same conditions as the reference model in Section 6.1. The results are shown in Fig. C.14(a).

Fig. C.14(a) shows the variation in the cavitation ratio with subsurface microstructure. The variation in correlation calculated was significant, ranging from 0.04 for the reference model from Section 6.1 to an absolute value of 0.78 for the textured substructure. This result outlines the significance of the effect of subsurface microstructure on damage initiation. Through the combined use of successive EBSD scans on new layers of material that is exposed by removing the top surface with a controlled focused ion beam, a full 3D microstructure could be reconstructed within this crystal plasticity framework. This result also shows that grain boundary misorientation, which in turn increases rates of carbide precipitation (Hong et al., 2001), can be seen as significant a factor in grain boundary damage initiation as the subsurface microstructure by comparison between the correlations in cavitation ratio. The stress strain response in each model was sufficiently similar to rule this out as a reason for differences in damage initiation, as well as the relation between grain boundary stress and phase field damage which was similar in each model (see Fig. E.17). The length-scale, l_0, used within Section 6.1 was 3 μm. Simulations were run over the reference simulation mesh with the same conditions other than varying length-scale. By increasing l_0 from 3 μm to up to 15 μm, the correlation in cavitation ratio against experimental data increased from 0.04 to up to 0.24. Upon comparison of the phase field across the microstructure, the increase in l_0 causes two main differences. The first is that the damage is higher across the entire microstructure, this is due to the terms in Eq. (25) dependent on the length-scale and the gradient of the damage parameter c. The second difference to note is that the phase field is more diffuse, with fewer distinguishable sharp features that can be mapped to the underlying grain boundaries within the starting microstructure. This result suggests that while changing the characteristic length-scale has an effect on the final phase field and the magnitude of the damage observed, the variation in damage initiation across the microstructure with grain boundaries of varying misorientation is not significantly changed (see Fig. E.18).

Appendix D. Combined creep and plastic deformation model images

See Figs. D.15 and D.16.

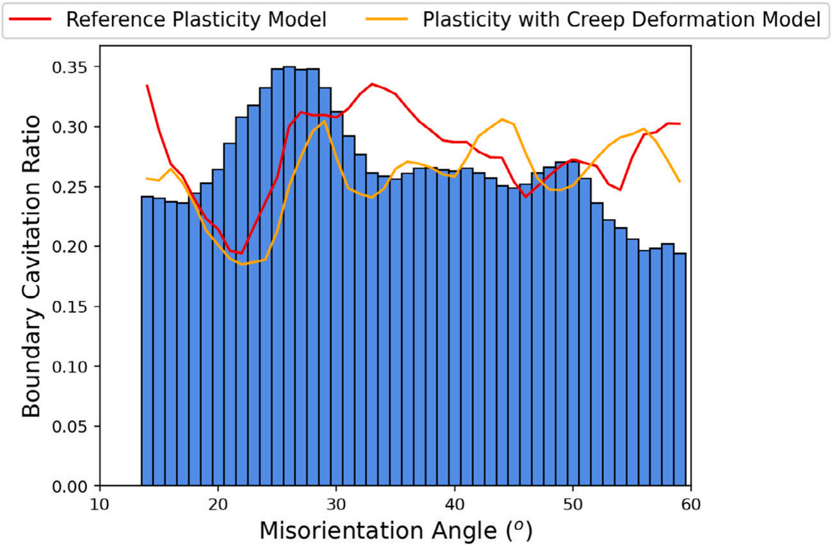

Fig. D.15. A histogram of the experimentally determined cavitation ratio against boundary misorientation angle in 316H stainless steel compared with the simulated data with the combined plastic slip creep model. The correlation was 0.35.

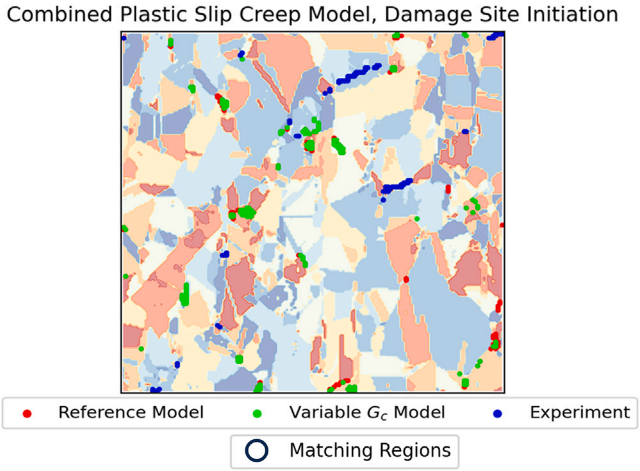

Fig. D.16. An EBSD microstructure overlaid with scatter plots of highly damaged regions within experimentally determined cavitation data as well a combined plastic slip and creep deformation crystal plasticity simulation. The regions of agreement between the damage model and experimental data are indicated.

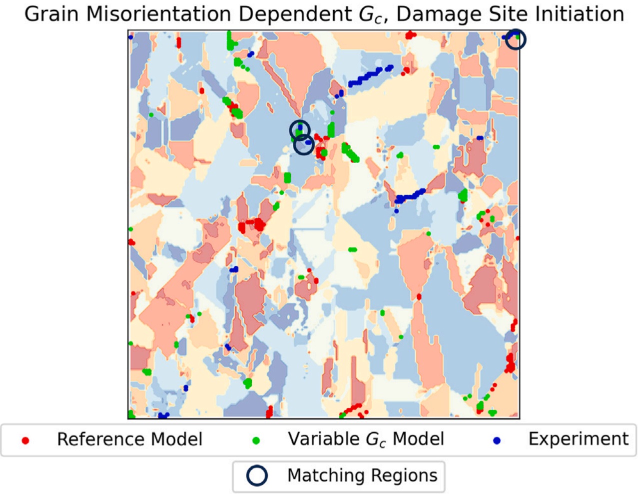

Fig. E.17. An EBSD microstructure overlaid with scatter plots of highly damaged regions within experimentally determined cavitation data as well a crystal plasticity simulation with the optimum misorientation dependent critical energy release rate implemented. The regions of agreement between the damage model and experimental data are indicated.

Appendix E. Damage spot comparison

See Figs. E.17 and E.18 for figures showing the change in damage spot prediction as a result of the implementation of the misorientation dependent critical energy release rate and elastoplastic damage model respectively. The regions where the implemented phase field model corresponds to regions of damage found experimentally have been marked.

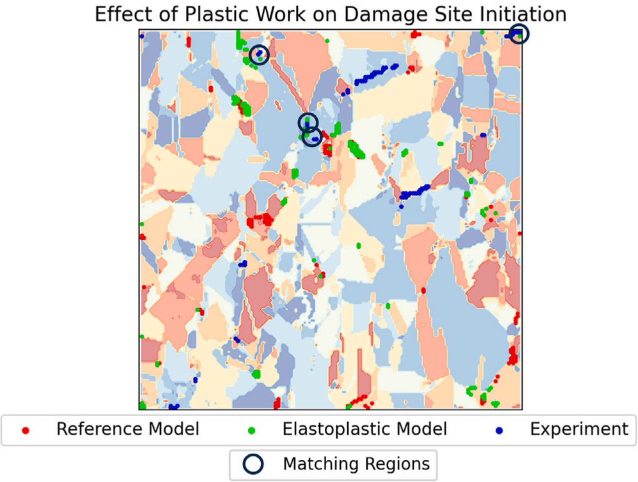

Fig. E.18. An EBSD image of the simulated microstructure, with scatter plots detailing grain boundaries meeting the damage threshold from the reference elastic strain energy damage model, the elastoplastic damage model, and experimentally determined cavitation data over the same microstructure. The regions of agreement between the damage model and experimental data are indicated.

Appendix F. Effect of increased strain on the phase field

To examine the effect of higher accumulated strain on the phase field, the simulations previously presented were repeated up to a higher strain in excess of the experimental conditions. This was to investigate whether the regions of damage within the phase field changes as the microstructure is subjected to higher strain. As can be seen from Fig. F.19, the damage features are sharper in definition in the reference simulation due to the gradient terms in Eq. (25) but it is still clearly visible that the same grain boundaries and regions of damage remain the same at the higher magnitude of the phase field between the two cases.

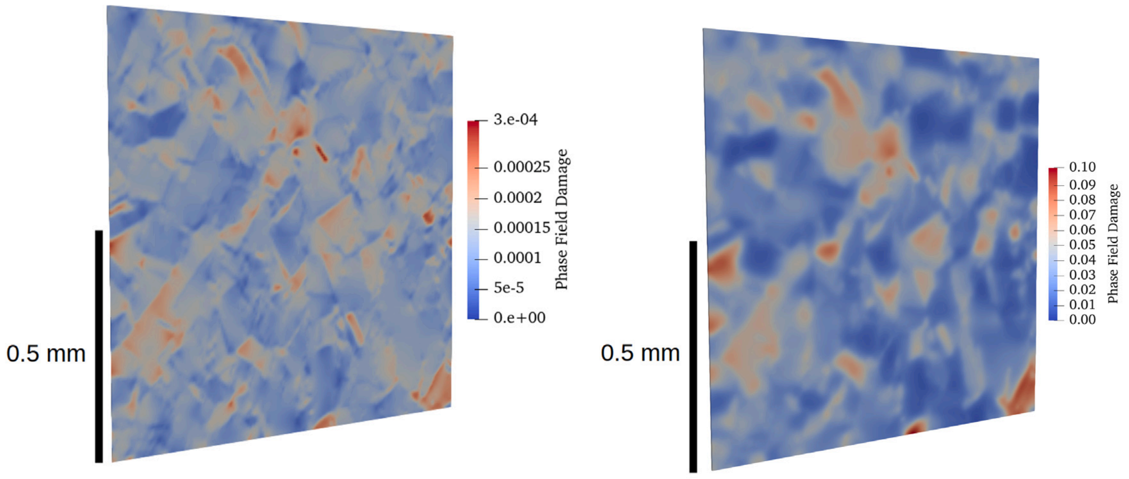

(a) (b)

Fig. F.19. Comparing the phase field from the same microstructure at 0.15% strain (a), and 3% strain to compare the effect of increased accumulated strain on the level of damage. It can be seen that at higher strain the phase field has fewer visible sharp features due to the increased contribution to local gradient terms at higher values of phase field damage, but that the regions where damage initiates in the lower strain simulation matches the same regions at higher strain.

References

Abdolvand, H., 2022. Development of microstructure-sensitive damage models for zirconium polycrystals. Int. J. Plast. 149, 103156. http://dx.doi.org/10.1016/j.ijplas.2021.103156, URL https://www.sciencedirect.com/science/article/pii/S0749641921002230.

Abrivard, G., Busso, E., Forest, S., Appolaire, B., 2012. Phase field modelling of grain boundary motion driven by curvature and stored energy gradients. Part I: theory and numerical implementation. Phil. Mag. 92 (28–30), 3618–3642. http://dx.doi.org/10.1080/14786435.2012.713135.

Agius, D., Kareer, A., Mamun, A.A., Truman, C., Collins, D.M., Mostafavi, M., Knowles, D., 2022. A crystal plasticity model that accounts for grain size effects and slip system interactions on the deformation of austenitic stainless steels. Int. J. Plast. 152, 103249. http://dx.doi.org/10.1016/j.ijplas.2022.103249, URL https://www.sciencedirect.com/science/article/pii/S0749641922000341.

Ali, M.A., Shchyglo, O., Stricker, M., Steinbach, I., 2023. Coherency loss marking the onset of degradation in high temperature creep of superalloys: Phase-field simulation coupled to strain gradient crystal plasticity. Comput. Mater. Sci. 220, 112069. http://dx.doi.org/10.1016/J.COMMATSCI.2023.112069.

Amor, H., Marigo, J.-J., Maurini, C., 2009. Regularized formulation of the variational brittle fracture with unilateral contact: Numerical experiments. J. Mech. Phys. Solids 57 (8), 1209–1229. http://dx.doi.org/10.1016/j.jmps.2009.04.011, URL https://www.sciencedirect.com/science/article/pii/S0022509609000659.

Arsenlis, A., Parks, D.M., 2002. Modeling the evolution of crystallographic dislocation density in crystal plasticity. J. Mech. Phys. Solids 50 (9), 1979–2009. http://dx.doi.org/10.1016/S0022-5096(01)00134-X, URL https://www.sciencedirect.com/science/article/pii/S002250960100134X.

Asaro, R., Rice, J., 1977. Strain localization in ductile single crystals. J. Mech. Phys. Solids 25 (5), 309–338. http://dx.doi.org/10.1016/0022-5096(77)90001-1, URL https://www.sciencedirect.com/science/article/pii/0022509677900011.

Ashby, M., 1970. The deformation of plastically non-homogeneous materials. Philos. Mag. A J. Theor. Exp. Appl. Phys. 21 (170), 399–424. http://dx.doi.org/10.1080/14786437008238426.

Ask, A., Forest, S., Appolaire, B., Ammar, K., 2019. A cosserat–phase-field theory of crystal plasticity and grain boundary migration at finite deformation. Contin. Mech. Thermodyn. 31 (4), 1109–1141. http://dx.doi.org/10.1007/S00161-018-0727-6/METRICS.

Asqardoust, S., Sarmah, A., Jain, M.K., Zurob, H.S., Kamat, R., 2023. Strain localization and damage development during elevated temperature deformation of AA7075 Aluminum sheet. Int. J. Plast. 161, 103513. http://dx.doi.org/10.1016/j.ijplas.2022.103513, URL https://www.sciencedirect.com/science/article/pii/S074964192200290X.

Balasubramanian, S., 1995. Polycrystalline Plasticity and Its Applications to Deformation Processing (Ph.D. thesis). Massachusetts Institute of Technology.

Bayley, C., Brekelmans, W., Geers, M., 2006. A comparison of dislocation induced back stress formulations in strain gradient crystal plasticity. Int. J. Solids Struct. 43 (24), 7268–7286. http://dx.doi.org/10.1016/j.ijsolstr.2006.05.011, Size-dependent Mechanics of Materials, URL https://www.sciencedirect.com/science/article/pii/S0020768306001697.

Bieberdorf, N., Tallman, A., Kumar, M.A., Taupin, V., Lebensohn, R.A., Capolungo, L., 2021. A mechanistic model for creep lifetime of ferritic steels: Application to Grade 91. Int. J. Plast. 147, 103086. http://dx.doi.org/10.1016/j.ijplas.2021.103086, URL https://www.sciencedirect.com/science/article/pii/S0749641921001571.

Borden, M.J., Hughes, T.J., Landis, C.M., Anvari, A., Lee, I.J., 2016. A phase-field formulation for fracture in ductile materials: Finite deformation balance law derivation, plastic degradation, and stress triaxiality effects. Comput. Methods Appl. Mech. Engrg. 312, 130–166. http://dx.doi.org/10.1016/j.cma.2016.09.005, Phase Field Approaches to Fracture, URL https://www.sciencedirect.com/science/article/pii/S0045782516311069.

Bouchard, P., Withers, P., McDonald, S., Heenan, R., 2004. Quantification of creep cavitation damage around a crack in a stainless steel pressure vessel. Acta Mater. 52 (1), 23–34. http://dx.doi.org/10.1016/j.actamat.2003.08.022, URL https://www.sciencedirect.com/science/article/pii/S1359645403005032.

Catalao, S., Feaugas, X., Pilvin, P., Cabrillat, M.-T., 2005. Dipole heights in cyclically deformed polycrystalline AISI 316L stainless steel. Mater. Sci. Eng. A 400–401, 349–352. http://dx.doi.org/10.1016/j.msea.2005.03.094, Dislocations 2004, URL https://www.sciencedirect.com/science/article/pii/S0921509305003242.

Chen, I.-W., Argon, A., 1981. Creep cavitation in 304 stainless steel. Acta Metall. 29 (7), 1321–1333. http://dx.doi.org/10.1016/0001-6160(81)90023-7, URL https://www.sciencedirect.com/science/article/pii/0001616081900237.

Chen, B., Flewitt, P.E., Smith, D.J., Jones, C.P., 2011. An improved method to identify grain boundary creep cavitation in 316H austenitic stainless steel. Ultramicroscopy 111, 309–313. http://dx.doi.org/10.1016/J.ULTRAMIC.2011.01.013.

Chockalingam, K., Tonks, M.R., Hales, J.D., Gaston, D.R., Millett, P.C., Zhang, L., 2013. Crystal plasticity with Jacobian-Free Newton–Krylov. Comput. Mech. 51 (5), 617–627. http://dx.doi.org/10.1007/s00466-012-0741-7, URL https://link.springer.com/article/10.1007/s00466-012-0741-7#citeas.

Cocks, A., Ashby, M., 1982. On creep fracture by void growth. Prog. Mater. Sci. 27 (3), 189–244. http://dx.doi.org/10.1016/0079-6425(82)90001-9, URL https://www.sciencedirect.com/science/article/pii/0079642582900019.

Das, S., Hofmann, F., Tarleton, E., 2018. Consistent determination of geometrically necessary dislocation density from simulations and experiments. Int. J. Plast. 109, 18–42. http://dx.doi.org/10.1016/j.ijplas.2018.05.001, URL https://www.sciencedirect.com/science/article/pii/S0749641918300068.

Demir, E., Horton, E.W., Kareer, A., Collins, D.M., Mostafavi, M., Knowles, D., 2023. A finite element method to calculate geometrically necessary dislocation density: Accounting for orientation discontinuities in polycrystals. Acta Mater. 245, 118658. http://dx.doi.org/10.1016/j.actamat.2022.118658, URL https://www.sciencedirect.com/science/article/pii/S1359645422010333.

Diehl, M., Wicke, M., Shanthraj, P., Roters, F., Brueckner-Foit, A., Raabe, D., 2017. Coupled crystal plasticity–phase field fracture simulation study on damage evolution around a void: Pore shape versus crystallographic orientation. JOM 69 (5), 872–878. http://dx.doi.org/10.1007/s11837-017-2308-8, URL https://link.springer.com/article/10.1007/s11837-017-2308-8.

Dittmann, M., Aldakheel, F., Schulte, J., Schmidt, F., Krüger, M., Wriggers, P., Hesch, C., 2020. Phase-field modeling of porous-ductile fracture in non-linear thermo-elasto-plastic solids. Comput. Methods Appl. Mech. Engrg. 361, 112730. http://dx.doi.org/10.1016/j.cma.2019.112730, URL https://www.sciencedirect.com/science/article/pii/S0045782519306206.

Duarte, C.A., Grilli, N., Koslowski, M., 2018. Effect of initial damage variability on hot-spot nucleation in energetic materials. J. Appl. Phys. 124 (2), 025104. http://dx.doi.org/10.1063/1.5030656.

Duarte, C.A., Koslowski, M., 2023. Hot-spots in polycrystalline β -tetramethylene tetranitramine (β -HMX): The role of plasticity and friction. J. Mech. Phys. Solids 171, 105157. http://dx.doi.org/10.1016/j.jmps.2022.105157, URL https://www.sciencedirect.com/science/article/pii/S0022509622003337.

Falgout, R.D., Yang, U.M., 2002. hypre: A library of high performance preconditioners. In: Sloot, P.M.A., Hoekstra, A.G., Tan, C.J.K., Dongarra, J.J. (Eds.), Computational Science — ICCS 2002. Springer Berlin Heidelberg, Berlin, Heidelberg, pp. 632–641.

Flint, T., Sun, Y., Xiong, Q., Smith, M., Francis, J., 2019. Phase-field simulation of grain boundary evolution in microstructures containing second-phase particles with heterogeneous thermal properties. Sci. Rep. 9, http://dx.doi.org/10.1038/s41598-019-54883-8.

Forget, P., Marini, B., Vincent, L., 2016. Application of local approach to fracture of an RPV steel: effect of the crystal plasticity on the critical carbide size. Procedia Struct. Integr. 2, 1660–1667. http://dx.doi.org/10.1016/j.prostr.2016.06.210, 21st European Conference on Fracture, ECF21, 20-24 June 2016, Catania, Italy, URL https://www.sciencedirect.com/science/article/pii/S2452321616302219.

Franciosi, P., Zaoui, A., 1982. Multislip in f.c.c. crystals a theoretical approach compared with experimental data. Acta Metall. 30 (8), 1627–1637. http://dx.doi.org/10.1016/0001-6160(82)90184-5, URL https://www.sciencedirect.com/science/article/pii/0001616082901845.

van der Giessen, E., Schultz, P.A., Bertin, N., Bulatov, V.V., Cai, W., Csányi, G., Foiles, S.M., Geers, M.G.D., González, C., Hütter, M., Kim, W.K., Kochmann, D.M., LLorca, J., Mattsson, A.E., Rottler, J., Shluger, A., Sills, R.B., Steinbach, I., Strachan, A., Tadmor, E.B., 2020. Roadmap on multiscale materials modeling. Modelling Simul. Mater. Sci. Eng. 28 (4), 043001. http://dx.doi.org/10.1088/1361-651X/ab7150.

Griffith, A.A., Taylor, G.I., 1921. VI. The phenomena of rupture and flow in solids. Philos. Trans. Royal Soc. Lond. Ser. A Contain. Pap. Math. Phys. Character 221 (582–593), 163–198. http://dx.doi.org/10.1098/rsta.1921.0006, arXiv:https://royalsocietypublishing.org/doi/pdf/10.1098/rsta.1921.0006, URL https://royalsocietypublishing.org/doi/abs/10.1098/rsta.1921.0006.

Grilli, N., 2016. Physics-Based Constitutive Modelling for Crystal Plasticity Finite Element Computation of Cyclic Plasticity in Fatigue (Ph.D. thesis). École Polytechnique Fédérale de Lausanne, http://dx.doi.org/10.5075/epfl-thesis-7251, URL https://infoscience.epfl.ch/record/223625.

Grilli, N., Cocks, A., Tarleton, E., 2019. Crystal plasticity finite element simulations of cast α-uranium. In: Onate, E., Owen, D., Peric, D., Chiumenti, M. (Eds.), Computational Plasticity XV: Fundamentals and Applications. http://dx.doi.org/10.1016/j.commatsci.2019.109276, 15th International Conference on Computational Plasticity - Fundamentals and Applications (COMPLAS), Barcelona, Spain, Sep 03-05, 2019, URL https://upcommons.upc.edu/handle/2117/181448.

Grilli, N., Cocks, A.C., Tarleton, E., 2020. Crystal plasticity finite element modelling of coarse-grained α-uranium. Comput. Mater. Sci. 171, 109276. http://dx.doi.org/10.1016/j.commatsci.2019.109276, URL https://www.sciencedirect.com/science/article/pii/S0927025619305750.

Grilli, N., Cocks, A.C.F., Tarleton, E., 2022a. Modelling the nucleation and propagation of cracks at twin boundaries. Int. J. Fract. 233 (1), 17–38. http://dx.doi.org/10.1007/s10704-021-00606-y, URL https://link.springer.com/article/10.1007/s10704-021-00606-y#citeas.

Grilli, N., Dandekar, A., Koslowski, M., 2017. Coupling crystal plasticity and phase-field damage to simulate β-HMX-based polymer-bonded explosive under shock load. In: APS Shock Compression of Condensed Matter Meeting Abstracts. In: APS Meeting Abstracts, p. Z4.002.

Grilli, N., Duarte, C.A., Koslowski, M., 2018a. Dynamic fracture and hot-spot modeling in energetic composites. J. Appl. Phys. 123 (6), 065101. http://dx.doi.org/10.1063/1.5009297.

Grilli, N., Hu, D., Yushu, D., Chen, F., Yan, W., 2022b. Crystal plasticity model of residual stress in additive manufacturing using the element elimination and reactivation method. Comput. Mech. 69, 825–845. http://dx.doi.org/10.1007/s00466-021-02116-z, URL https://link.springer.com/article/10.1007/s00466-021-02116-z#citeas.

Grilli, N., Janssens, K., Nellessen, J., Sandlöbes, S., Raabe, D., 2018b. Multiple slip dislocation patterning in a dislocation-based crystal plasticity finite element method. Int. J. Plast. 100, 104–121. http://dx.doi.org/10.1016/j.ijplas.2017.09.015, URL https://www.sciencedirect.com/science/article/pii/S0749641917305570.

Grilli, N., Janssens, K.G., Van Swygenhoven, H., 2015. Crystal plasticity finite element modelling of low cycle fatigue in fcc metals. J. Mech. Phys. Solids 84, 424–435. http://dx.doi.org/10.1016/j.jmps.2015.08.007, URL https://www.sciencedirect.com/science/article/pii/S0022509615300727.

Grilli, N., Koslowski, M., 2018. The effect of crystal orientation on shock loading of single crystal energetic materials. Comput. Mater. Sci. 155, 235–245. http://dx.doi.org/10.1016/j.commatsci.2018.08.059.

Grilli, N., Koslowski, M., 2019. The effect of crystal anisotropy and plastic response on the dynamic fracture of energetic materials. J. Appl. Phys. 126 (15), 155101. http://dx.doi.org/10.1063/1.5109761.

Grilli, N., Salvini, M., 2022. Pydakota. In: GitHub Repository. GitHub, https://github.com/ngrilli/PyDakota.

Grilli, N., Tarleton, E., Cocks, A.C.F., 2021a. Coupling a discrete twin model with cohesive elements to understand twin-induced fracture. Int. J. Fract. 227 (2), 173–192. http://dx.doi.org/10.1007/s10704-020-00504-9.

Grilli, N., Tarleton, E., Cocks, A.C., 2021b. Neper2CAE and PyCiGen: Scripts to generate polycrystals and interface elements in abaqus. SoftwareX 13, 100651. http://dx.doi.org/10.1016/j.softx.2020.100651, URL https://www.sciencedirect.com/science/article/pii/S2352711020303642.

Gupta, S., Bronkhorst, C.A., 2021. Crystal plasticity model for single crystal Ni-based superalloys: Capturing orientation and temperature dependence of flow stress. Int. J. Plast. 137, 102896. http://dx.doi.org/10.1016/j.ijplas.2020.102896, URL https://www.sciencedirect.com/science/article/pii/S0749641920304332.

Gurson, A.L., 1977. Continuum theory of ductile rupture by void nucleation and growth: Part I—Yield criteria and flow rules for porous ductile media. J. Eng. Mater. Technol. 99 (1), 2–15. http://dx.doi.org/10.1115/1.3443401, arXiv:https://asmedigitalcollection.asme.org/materialstechnology/article-pdf/99/1/2/5788715/2_1.pdf.

Hao, S., Brocks, W., 1997. The Gurson-Tvergaard-Needleman-model for rate and temperature-dependent materials with isotropic and kinematic hardening. Comput. Mech. 20 (1), 34–40. http://dx.doi.org/10.1007/s004660050213, URL https://link.springer.com/article/10.1007/s004660050213#citeas.

He, S., Horton, E., Moore, S., Fernandez-Caballero, A., Elmukashf, E., Salvini, M., Flewitt, P., Knowles, D., Mostafavi, M., Martin, T., 2023. A correlative approach to evaluating the links between local microstructural parameters and creep initiated cavities (submitted to Materials & Design for publication).

He, S., Shang, H., Fernández-Caballero, A., Warren, A., Knowles, D., Flewitt, P., Martin, T., 2021. The role of grain boundary ferrite evolution and thermal aging on creep cavitation of type 316H austenitic stainless steel. Mater. Sci. Eng. A 807, 140859. http://dx.doi.org/10.1016/j.msea.2021.140859, URL https://www.sciencedirect.com/science/article/pii/S0921509321001283.

Hidalgo, J., Vittorietti, M., Farahani, H., Vercruysse, F., Petrov, R., Sietsma, J., 2020. Influence of M23C6 carbides on the heterogeneous strain development in annealed 420 stainless steel. Acta Mater. 200, 74–90. http://dx.doi.org/10.1016/j.actamat.2020.08.072, URL https://www.sciencedirect.com/science/article/pii/S1359645420306820.

Hielscher, R., Schaeben, H., 2008. A novel pole figure inversion method: specification of the *MTEX* algorithm. J. Appl. Crystallogr. 41 (6), 1024–1037. http://dx.doi.org/10.1107/S0021889808030112.

Hong, H.U., Rho, B.S., Nam, S.W., 2001. Correlation of the M23C6 precipitation morphology with grain boundary characteristics in austenitic stainless steel. Mater. Sci. Eng. A 318, 285–292. http://dx.doi.org/10.1016/S0921-5093(01)01254-0.

Hu, D., Grilli, N., Wang, L., Yang, M., Yan, W., 2022. Microscale residual stresses in additively manufactured stainless steel: Computational simulation. J. Mech. Phys. Solids 161, 104822. http://dx.doi.org/10.1016/j.jmps.2022.104822, URL https://www.sciencedirect.com/science/article/pii/S0022509622000394.

Hu, D., Grilli, N., Yan, W., 2023. Dislocation structures formation induced by thermal stress in additive manufacturing: Multiscale crystal plasticity modeling of dislocation transport. J. Mech. Phys. Solids 173, 105235. http://dx.doi.org/10.1016/j.jmps.2023.105235, URL https://www.sciencedirect.com/science/article/pii/S002250962300039X.

Irastorza-Landa, A., Grilli, N., Swygenhoven, H.V., 2017a. Effect of pre-existing immobile dislocations on the evolution of geometrically necessary dislocations during fatigue. Modelling Simul. Mater. Sci. Eng. 25 (5), 055010. http://dx.doi.org/10.1088/1361-651X/aa6e24.

Irastorza-Landa, A., Grilli, N., Van Swygenhoven, H., 2017b. Laue micro-diffraction and crystal plasticity finite element simulations to reveal a vein structure in fatigued Cu. J. Mech. Phys. Solids 104, 157–171. http://dx.doi.org/10.1016/j.jmps.2017.04.010, URL https://www.sciencedirect.com/science/article/pii/S0022509616304781.

Isfandbod, M., Martínez-Pañeda, E., 2021. A mechanism-based multi-trap phase field model for hydrogen assisted fracture. Int. J. Plast. 144, 103044. http://dx.doi.org/10.1016/j.ijplas.2021.103044, URL https://www.sciencedirect.com/science/article/pii/S0749641921001182.

Jones, R., Randle, V., Owen, G., 2008. Carbide precipitation and grain boundary plane selection in overaged type 316 austenitic stainless steel. Mater. Sci. Eng. A 496, 256–261. http://dx.doi.org/10.1016/J.MSEA.2008.05.028.

Kalidindi, S.R., 1998. Incorporation of deformation twinning in crystal plasticity models. J. Mech. Phys. Solids 46 (2), 267–290. http://dx.doi.org/10.1016/S0022-5096(97)00051-3, URL https://www.sciencedirect.com/science/article/pii/S0022509697000513.

Kalidindi, S., Bronkhorst, C., Anand, L., 1992. Crystallographic texture evolution in bulk deformation processing of FCC metals. J. Mech. Phys. Solids 40 (3), 537–569. http://dx.doi.org/10.1016/0022-5096(92)80003-9, URL https://www.sciencedirect.com/science/article/pii/0022509692800039.

Kristensen, P.K., Niordson, C.F., Martínez-Pañeda, E., 2021. An assessment of phase field fracture: crack initiation and growth. Phil. Trans. R. Soc. A 379 (2203), 20210021. http://dx.doi.org/10.1098/rsta.2021.0021, arXiv:https://royalsocietypublishing.org/doi/pdf/10.1098/rsta.2021.0021, URL https://royalsocietypublishing.org/doi/abs/10.1098/rsta.2021.0021.

Kumar, A., Bourdin, B., Francfort, G.A., Lopez-Pamies, O., 2020. Revisiting nucleation in the phase-field approach to brittle fracture. J. Mech. Phys. Solids 142, 104027. http://dx.doi.org/10.1016/j.jmps.2020.104027, URL https://www.sciencedirect.com/science/article/pii/S0022509620302623.

Lee, E.H., 1969. Elastic-Plastic Deformation at Finite Strains. J. Appl. Mech. 36 (1), 1–6. http://dx.doi.org/10.1115/1.3564580, arXiv:https://asmedigitalcollection.asme.org/appliedmechanics/article-pdf/36/1/1/5449476/1_1.pdf.

Li, C., Fang, J., Wu, C., Sun, G., Steven, G., Li, Q., 2022a. Phase field fracture in elasto-plastic solids: Incorporating phenomenological failure criteria for ductile materials. Comput. Methods Appl. Mech. Engrg. 391, 114580. http://dx.doi.org/10.1016/j.cma.2022.114580, URL https://www.sciencedirect.com/science/article/pii/S0045782522000068.

Li, Z., Wang, T., Chu, D., Liu, Z., Cui, Y., 2022b. A coupled crystal-plasticity and phase-field model for understanding fracture behaviors of single crystal tungsten. Int. J. Plast. 157, 103375. http://dx.doi.org/10.1016/j.ijplas.2022.103375, URL https://www.sciencedirect.com/science/article/pii/S0749641922001553.

Li, K.-S., Wang, R.-Z., Zhang, X.-C., Tu, S.-T., 2023. Creep-fatigue damage mechanisms and life prediction based on crystal plasticity combined with grain boundary cavity model in a nickel-based superalloy at 650°C. Int. J. Plast. 165, 103601. http://dx.doi.org/10.1016/j.ijplas.2023.103601, URL https://www.sciencedirect.com/science/article/pii/S0749641923000876.

Lian, J., Yang, H., Vajragupta, N., Münstermann, S., Bleck, W., 2014. A method to quantitatively upscale the damage initiation of dual-phase steels under various stress states from microscale to macroscale. Comput. Mater. Sci. 94, 245–257. http://dx.doi.org/10.1016/j.commatsci.2014.05.051, IWCMM23 Special Issue, URL https://www.sciencedirect.com/science/article/pii/S0927025614003772.

Lu, J., Sun, W., Becker, A., 2016. Material characterisation and finite element modelling of cyclic plasticity behaviour for 304 stainless steel using a crystal plasticity model. Int. J. Mech. Sci. 105, 315–329. http://dx.doi.org/10.1016/j.ijmecsci.2015.11.024, URL https://www.sciencedirect.com/science/article/pii/S0020740315004014.

Martin, T., He, S., Horton, E., Shang, H., Fernandez-Caballero, A., Grilli, N., Mostafavi, M., Knowles, D., Cocks, A., Flewitt, P., et al., 2022. New correlative microscopy approaches to understand the microstructural origins of creep cavitation in austenitic steels. Microsc. Microanal. 28 (S1), 2074–2075. http://dx.doi.org/10.1017/S1431927622008030.

Martin, T.L., He, S., Warren, A.D., Shang, H., Knowles, D.M., Flewitt, P.E.J., 2020. The role of grain boundary orientation and secondary phases in creep cavity nucleation of a 316H boiler header. In: Pressure Vessels and Piping Conference. In: Materials and Fabrication, vol. 6, http://dx.doi.org/10.1115/PVP2020-21791, V006T06A043, arXiv:https://asmedigitalcollection.asme.org/PVP/proceedings-pdf/PVP2020/83860/V006T06A043/6583908/v006t06a043-pvp2020-21791.pdf.

Mehmanparast, A., Davies, C., Dean, D., Nikbin, K., 2013. The influence of pre-compression on the creep deformation and failure behaviour of Type 316H stainless steel. Eng. Fract. Mech. 110, 52–67. http://dx.doi.org/10.1016/j.engfracmech.2013.08.006, URL https://www.sciencedirect.com/science/article/pii/S0013794413002725.

Mianroodi, J.R., Shanthraj, P., Liu, C., Vakili, S., Roongta, S., Siboni, N.H., Perchikov, N., Bai, Y., Svendsen, B., Roters, F., Raabe, D., Diehl, M., 2022. Modeling and simulation of microstructure in metallic systems based on multi-physics approaches. npj Comput. Mater. 8, 93. http://dx.doi.org/10.1038/s41524-022-00764-0, URL https://www.nature.com/articles/s41524-022-00764-0#citeas.

Miehe, C., Hofacker, M., Schänzel, L.-M., Aldakheel, F., 2015a. Phase field modeling of fracture in multi-physics problems. Part II. coupled brittle-to-ductile failure criteria and crack propagation in thermo-elastic–plastic solids. Comput. Methods Appl. Mech. Engrg. 294, 486–522. http://dx.doi.org/10.1016/j.cma.2014.11.017, URL https://www.sciencedirect.com/science/article/pii/S0045782514004435.

Miehe, C., Schänzel, L.-M., Ulmer, H., 2015b. Phase field modeling of fracture in multi-physics problems. Part I. Balance of crack surface and failure criteria for brittle crack propagation in thermo-elastic solids. Comput. Methods Appl. Mech. Engrg. 294, 449–485. http://dx.doi.org/10.1016/j.cma.2014.11.016, URL https://www.sciencedirect.com/science/article/pii/S0045782514004423.

Miehe, C., Welschinger, F., Hofacker, M., 2010a. Thermodynamically consistent phase-field models of fracture: Variational principles and multi-field FE implementations. Internat. J. Numer. Methods Engrg. 83 (10), 1273–1311. http://dx.doi.org/10.1002/nme.2861, URL https://onlinelibrary.wiley.com/doi/abs/10.1002/nme.2861, arXiv:https://onlinelibrary.wiley.com/doi/pdf/10.1002/nme.2861.

Miehe, C., Welschinger, F., Hofacker, M., 2010b. Thermodynamically consistent phase-field models of fracture: Variational principles and multi-field FE implementations. Internat. J. Numer. Methods Engrg. 83 (10), 1273–1311. http://dx.doi.org/10.1002/nme.2861, arXiv:https://onlinelibrary.wiley.com/doi/pdf/10.1002/nme.2861, URL https://onlinelibrary.wiley.com/doi/abs/10.1002/nme.2861.

Morris, D.G., Harries, D.R., 1977. Wedge crack nucleation in Type 316 stainless steel. J. Mater. Sci. 12 (8), 1587–1597. http://dx.doi.org/10.1007/BF00542809.

Pai, N., Prakash, A., Samajdar, I., Patra, A., 2022. Study of grain boundary orientation gradients through combined experiments and strain gradient crystal plasticity modeling. Int. J. Plast. 156, 103360. http://dx.doi.org/10.1016/j.ijplas.2022.103360, URL https://www.sciencedirect.com/science/article/pii/S0749641922001401.

Pang, Y., Grilli, N., Su, H., Liu, W., Ma, J., Yu, S.F., 2022. Experimental investigation on microstructures and mechanical properties of PG4 flash-butt rail welds. Eng. Fail. Anal. 141, 106650. http://dx.doi.org/10.1016/j.engfailanal.2022.106650, URL https://www.sciencedirect.com/science/article/pii/S1350630722006227.

Pantleon, W., 2008. Resolving the geometrically necessary dislocation content by conventional electron backscattering diffraction. Scr. Mater. 58 (11), 994–997. http://dx.doi.org/10.1016/j.scriptamat.2008.01.050, URL https://www.sciencedirect.com/science/article/pii/S1359646208000912.

Permann, C.J., Gaston, D.R., Andra, D., Carlsen, R.W., Kong, F., Lindsay, A.D., Miller, J.M., Peterson, J.W., Slaughter, A.E., Stogner, R.H., Martineau, R.C., 2020. MOOSE: Enabling massively parallel multiphysics simulation. SoftwareX 11, 100430. http://dx.doi.org/10.1016/j.softx.2020.100430, URL https://www.sciencedirect.com/science/article/pii/S2352711019302973.

Petkov, M., Cocks, A., 2020. Modelling Microstructure Evolution, Creep Deformation and Damage in Type 316H Stainless Steel (Ph.D. thesis).

Petkov, M.P., Hu, J., Tarleton, E., Cocks, A.C., 2019. Comparison of self-consistent and crystal plasticity FE approaches for modelling the high-temperature deformation of 316H austenitic stainless steel. Int. J. Solids Struct. 171, 54–80. http://dx.doi.org/10.1016/j.ijsolstr.2019.05.006, URL https://www.sciencedirect.com/science/article/pii/S002076831930229X.

Pommier, H., Busso, E.P., Morgeneyer, T.F., Pineau, A., 2016. Intergranular damage during stress relaxation in AISI 316L-type austenitic stainless steels: Effect of carbon, nitrogen and phosphorus contents. Acta Mater. 103, 893–908. http://dx.doi.org/10.1016/J.ACTAMAT.2015.11.004.

Prahs, A., Schöller, L., Schwab, F.K., Schneider, D., Böhlke, T., Nestler, B., 2023. A multiphase-field approach to small strain crystal plasticity accounting for balance equations on singular surfaces. Comput. Mech. 1–22. http://dx.doi.org/10.1007/S00466-023-02389-6/FIGURES/9.

Price, A., Smith, M.C., Dennis, R., Spindler, M.W., 2009. Revised weld residual stress and creep damage assessments. In: Pressure Vessels and Piping Conference. In: Materials and Fabrication, Parts A and B, vol. 6, pp. 559–568. http://dx.doi.org/10.1115/PVP2009-77960, arXiv:https://asmedigitalcollection.asme.org/PVP/proceedings-pdf/PVP2009/43697/559/4592035/559_1.pdf.

Ragab, R., Pang, Y., Liu, T., Neate, N., Li, M., Sun, W., 2023. Unravelling the effects of ratcheting and constraint on the cyclic behaviour of a martensitic steel under elevated temperature. Mech. Mater. 184, 104708. http://dx.doi.org/10.1016/j.mechmat.2023.104708, URL https://www.sciencedirect.com/science/article/pii/S0167663623001540.

Rice, J., 1971. Inelastic constitutive relations for solids: An internal-variable theory and its application to metal plasticity. J. Mech. Phys. Solids 19 (6), 433–455. http://dx.doi.org/10.1016/0022-5096(71)90010-X, URL https://www.sciencedirect.com/science/article/pii/002250967190010X.

Roters, F., Diehl, M., Shanthraj, P., Eisenlohr, P., Reuber, C., Wong, S., Maiti, T., Ebrahimi, A., Hochrainer, T., Fabritius, H.-O., Nikolov, S., Friák, M., Fujita, N., Grilli, N., Janssens, K., Jia, N., Kok, P., Ma, D., Meier, F., Werner, E., Stricker, M., Weygand, D., Raabe, D., 2019. DAMASK – the Düsseldorf Advanced Material Simulation Kit for modeling multi-physics crystal plasticity, thermal, and damage phenomena from the single crystal up to the component scale. Comput. Mater. Sci. 158, 420–478. http://dx.doi.org/10.1016/j.commatsci.2018.04.030, URL https://www.sciencedirect.com/science/article/pii/S0927025618302714.

Sandström, R., He, J.-J., 2022. Prediction of creep ductility for austenitic stainless steels and copper. Mater. High Temp. 39 (6), 427–435. http://dx.doi.org/10.1080/09603409.2022.2039497.

Sawada, K., Kimura, K., Abe, F., Taniuchi, Y., Sekido, K., Nojima, T., Ohba, T., Kushima, H., Miyazaki, H., Hongo, H., Watanabe, T., 2019. Catalog of NIMS creep data sheets. Sci. Technol. Adv. Mater. 20 (1), 1131–1149. http://dx.doi.org/10.1080/14686996.2019.1697616, PMID: 32082436.

Schöller, L., Schneider, D., Herrmann, C., Prahs, A., Nestler, B., 2022. Phase-field modeling of crack propagation in heterogeneous materials with multiple crack order parameters. Comput. Methods Appl. Mech. Engrg. 395, 114965. http://dx.doi.org/10.1016/J.CMA.2022.114965.

Sistaninia, M., Niffenegger, M., 2014. Prediction of damage-growth based fatigue life of polycrystalline materials using a microstructural modeling approach. Int. J. Fatigue 66, 118–126. http://dx.doi.org/10.1016/j.ijfatigue.2014.03.018, URL https://www.sciencedirect.com/science/article/pii/S0142112314001005.

Skamniotis, C., Grilli, N., Cocks, A.C., 2023. Crystal plasticity analysis of fatigue-creep behavior at cooling holes in single crystal Nickel based gas turbine blade components. Int. J. Plast. 166, 103589. http://dx.doi.org/10.1016/j.ijplas.2023.103589, URL https://www.sciencedirect.com/science/article/pii/S074964192300075X.

Slater, T.J.A., Bradley, R.S., Bertali, G., Geurts, R., Northover, S.M., Burke, M.G., Haigh, S.J., Burnett, T.L., Withers, P.J., 2017. Multiscale correlative tomography: an investigation of creep cavitation in 316 stainless steel. Sci. Rep. 7 (1), 7332. http://dx.doi.org/10.1038/s41598-017-06976-5, URL https://www.nature.com/articles/s41598-017-06976-5.

Tasan, C., Hoefnagels, J., Diehl, M., Yan, D., Roters, F., Raabe, D., 2014. Strain localization and damage in dual phase steels investigated by coupled in-situ deformation experiments and crystal plasticity simulations. Int. J. Plast. 63, 198–210. http://dx.doi.org/10.1016/j.ijplas.2014.06.004, Deformation Tensors in Material Modeling in Honor of Prof. Otto T. Bruhns, URL https://www.sciencedirect.com/science/article/pii/S0749641914001260.

Vasileiou, A.N., Smith, M.C., Francis, J.A., Balakrishnan, J., Wang, Y.L., Obasi, G., Burke, M.G., Pickering, E.J., Gandy, D.W., Irvine, N.M., 2021. Development of microstructure and residual stress in electron beam welds in low alloy pressure vessel steels. Mater. Des. 209, 109924. http://dx.doi.org/10.1016/j.matdes.2021.109924, URL https://www.sciencedirect.com/science/article/pii/S0264127521004779.

Vo, H., Frazer, D., Kohnert, A., Teysseyre, S., Fensin, S., Hosemann, P., 2023. Role of low-level void swelling on plasticity and failure in a 33 dpa neutron-irradiated 304 stainless steel. Int. J. Plast. 164, 103577. http://dx.doi.org/10.1016/j.ijplas.2023.103577, URL https://www.sciencedirect.com/science/article/pii/S0749641923000633.

Williams, R.J., Al-Lami, J., Hooper, P.A., Pham, M.-S., Davies, C.M., 2021. Creep deformation and failure properties of 316 L stainless steel manufactured by laser powder bed fusion under multiaxial loading conditions. Addit. Manuf. 37, 101706. http://dx.doi.org/10.1016/j.addma.2020.101706, URL https://www.sciencedirect.com/science/article/pii/S2214860420310782.

Xiao, X., Li, S., Yu, L., 2022. A general steady-state creep model incorporating dislocation static recovery for pure metallic materials. Int. J. Plast. 157, 103394. http://dx.doi.org/10.1016/j.ijplas.2022.103394, URL https://www.sciencedirect.com/science/article/pii/S0749641922001735.

Xiong, Y., Grilli, N., Karamched, P.S., Li, B.-S., Tarleton, E., Wilkinson, A.J., 2022. Cold dwell behaviour of ti6al alloy: Understanding load shedding using digital image correlation and dislocation based crystal plasticity simulations. J. Mater. Sci. Technol. 128, 254–272. http://dx.doi.org/10.1016/j.jmst.2022.05.034, URL https://www.sciencedirect.com/science/article/pii/S1005030222004881.

Xiong, Y., Karamched, P.S., Nguyen, C.-T., Collins, D.M., Grilli, N., Magazzeni, C.M., Tarleton, E., Wilkinson, A.J., 2021. An in-situ synchrotron diffraction study of stress relaxation in titanium: Effect of temperature and oxygen on cold dwell fatigue. Acta Mater. 213, 116937. http://dx.doi.org/10.1016/j.actamat.2021.116937, URL https://www.sciencedirect.com/science/article/pii/S1359645421003177.

Yalçinkaya, T., Tandoğan, İ., Özdemir, İ., 2021. Void growth based inter-granular ductile fracture in strain gradient polycrystalline plasticity. Int. J. Plast. 147, 103123. http://dx.doi.org/10.1016/j.ijplas.2021.103123, URL https://www.sciencedirect.com/science/article/pii/S0749641921001911.

Yavari, P., Langdon, T.G., 1983. Cavitation in high purity aluminium during fatigue at elevated temperatures. J. Mater. Sci. Lett. 2, 522–524.

You, X., Yang, J., Dan, C., Shi, Q., Zhong, S., Wang, H., Chen, Z., 2023. Statistical analysis of slip transfer in Al alloy based on in-situ tensile test and high-throughput computing method. Int. J. Plast. 166, 103649. http://dx.doi.org/10.1016/j.ijplas.2023.103649, URL https://www.sciencedirect.com/science/article/pii/S0749641923001353.

Zauter, R., Christ, H.J., Mughrabi, H., 1994. Some aspects of thermomechanical fatigue of AISI 304L stainless steel: Part I. creep- fatigue damage. Metall. Mater. Trans. A 25, 401–406. http://dx.doi.org/10.1007/BF02647985, URL https://link.springer.com/article/10.1007/BF02647985#citeas.

Zhang, Z., Thaulow, C., Ødegård, J., 2000. A complete gurson model approach for ductile fracture. Eng. Fract. Mech. 67 (2), 155–168. http://dx.doi.org/10.1016/S0013-7944(00)00055-2, URL https://www.sciencedirect.com/science/article/pii/S0013794400000552.

Zhang, S., Wang, L., Zhu, G., Diehl, M., Maldar, A., Shang, X., Zeng, X., 2022. Predicting grain boundary damage by machine learning. Int. J. Plast. 150, 103186. http://dx.doi.org/10.1016/j.ijplas.2021.103186, URL https://www.sciencedirect.com/science/article/pii/S0749641921002527.

Zhang, X., Zhao, J., Kang, G., Zaiser, M., 2023. Geometrically necessary dislocations and related kinematic hardening in gradient grained materials: A nonlocal crystal plasticity study. Int. J. Plast. 163, 103553. http://dx.doi.org/10.1016/j.ijplas.2023.103553, URL https://www.sciencedirect.com/science/article/pii/S0749641923000396.

Ziegler, H. (Ed.), 1983. An Introduction to Thermomechanics. In: North-Holland Series in Applied Mathematics and Mechanics, vol. 21, North-Holland, http://dx.doi.org/10.1016/B978-0-444-86503-8.50002-0, URL https://www.sciencedirect.com/science/article/pii/B9780444865038500020.

Zinkle, S.J., Was, G.S., 2013. Materials challenges in nuclear energy. Acta Mater. 61, 735–758. http://dx.doi.org/10.1016/J.ACTAMAT.2012.11.004.